Bangor University

MASTERS BY RESEARCH

El Niño-induced upwelling variability in the central tropical Pacific Ocean.

Guillaume-Castel, Robin

Award date:
2021

Awarding institution:
Bangor University

[Link to publication](#)

MASTERS BY RESEARCH

El Niño-induced upwelling variability in the central tropical Pacific Ocean.

Guillaume-Castel, Robin

Award date:
2021

Link to publication

El Niño-induced upwelling variability in the central tropical Pacific Ocean.

THESIS SUBMITTED FOR THE DEGREE OF MSCRES
ROBIN GUILLAUME-CASTEL

Under the supervision of Drs.
J.A. MATTIAS GREEN, ADEL HEENAN and **GARETH J. WILLIAMS**

Contact: r.guilcas@outlook.com

PRIFYSGOL
BANGOR
UNIVERSITY

ÉCOLE
POLYTECHNIQUE

IP PARIS

Abstract

Coral reefs are extremely sensitive ecosystems to climate change and especially to the warming oceans. Since 1980, three massive El Niño-associated heat stress periods triggered widespread bleaching events in the tropical Pacific that sometimes led to coral mortality. The understanding of potentially mitigating phenomena is crucial to choose where to focus conservation efforts. Through its capacity to bring cool, nutrient-enriched water in the warm oligotrophic shallows, upwelling can provide heat shelters for nearshore ecosystems. Little is known about the dynamics of upwelling during El Niño in the central tropical Pacific. Using ten years of subsurface temperature data and a thermocline depth reanalysis product, we here study the interconnections between upwelling intensity, thermocline depth and El Niño events in the central tropical Pacific.

Previous methods were designed to quantify upwelling dynamics, in terms of cold-water intrusion in the warm shallows or cold pulses. However, these often lack the ability to identify individual events, are parameter heavy, which means they require knowledge on the local hydrography, and are unable to differentiate the physical processes inducing the cooling event. Here, we first developed a new, automated and locally adapted detection method based on a temperature stratification index. Not only our algorithm solves issues encountered by the previous methods as it is automatically tuned to the local environment, it does not require any parameter, and it separates upwelling from other processes, but we show that it improves the detection rate by 10% compared to previously published methods.

Using our newly developed method, we quantified upwelling dynamics in ten years of subsurface temperature at five locations in the U.S. unaffiliated territory of the Pacific Remote Island Area. We observed extreme upwelling events at all five locations, and we show that these events are feature of strong and very strong El Niño events and their following La Niña as (1) they produce thermocline shoaling patterns and (2) shallow thermoclines are associated with intensified upwelling periods. Overall, our results show that El Niño and La Niña can produce temporary upwelling-exposed areas that act as shelters for nearshore ecosystems during intense heat stress. On the contrary, El Niño can also inhibit upwelling in previously exposed areas, temporary redistributing potential shelters. The understanding of the thermocline shoaling patterns during El Niño could provide geographical locations that could be naturally protected during El Niño and are therefore worthy of conservation efforts.

First page photography by Francesco Ungaro on pexels.com.

Contents

List of Figures

List of Tables

Acknowledgements

Chapter I. Introduction

Coral reefs are arguably some of the most threatened tropical marine ecosystems in our changing climate (Hoegh-Guldberg 1999). Corals are indeed highly sensitive to the properties of the sea water in which they live and slight deviations from the normal physicochemical properties of their environment, such as the lack of oxygen (Altieri et al. 2017), a lowered water pH (Hoegh-Guldberg et al. 2007; Manzello 2010) or an increased temperature (Hughes et al. 2017) can have dramatic effects on the reefs. When corals undergo warmer temperature than usual, their endosymbiont algae can be expelled and the corals bleach, leaving them without one of their main sources of nutrients which was provided by the algae through photosynthesis. If the corals remain bleached for too long, this can lead to their mortality (Glynn 1984; Vargas-Ángel et al. 2011; Furby et al. 2017; Sakai et al. 2019). Since our oceans are warming globally, increasing temperature is probably the biggest threat to coral reefs worldwide.

El Niño Southern Oscillation (ENSO) is a climate mode affecting winds, precipitations, temperature and other physical properties of the global climate (Zhang and McPhaden 2006; McPhaden et al. 2011). ENSO redistributes surface water in the tropical Pacific and Indian oceans, oscillating between a warm El Niño phase and a cooler La Niña (Trenberth 1997). El Niño is noticeably characterised by a warming of the tropical Pacific, reaching temperature several degrees warmer than the climatology. Since 1980, three massive El Niño events induced basin-wide heatwaves in the tropical Pacific, leading to the most widespread coral bleaching events on record (Hughes et al. 2017; Donner et al. 2017), first in 1982 (Glynn 1984), then in 1997 (Williams et al. 2010; Vargas-Ángel et al. 2011; Furby et al. 2017) and in 2015 (Hughes et al. 2017; Fox et al. 2019; Vargas-Ángel et al. 2019). El Niño events are planned to increase in both frequency and magnitude (Yeh et al. 2009), threatening even more coral reefs environments. Therefore, it appears crucial to understand and quantify potential mitigating processes that could provide support to coral reefs during intense heat stress.

In the tropical Pacific, the thermocline separates a warm, nutrient-depleted surface layer from a cool, nutrient-enriched deeper water. Upwelling is a process that can bring sub-thermocline water up in the shallows (Ross and Sharples 2007), allowing the transport of nutrients and other components of the deeper layer (Leichter et al. 1996; Sevadjian et al. 2012). Upwelling can be generated through several processes, like shoaling internal gravity waves, that propagate on the thermocline and break when they encounter bathymetry (Walter et al. 2012; Sutherland et al. 2013; Woodson 2018), or through a deep-water current that is topographically steered up, as the Equatorial Undercurrent shallows (Gove et al. 2006). Upwelling widely affects nearshore ecosystems, and noticeably coral reefs, as it can considerably

change the properties of the water when it brings cooler, nutrient-rich water in the warm oligotrophic surface environment. This way, upwelling can affect the spatial organisation (Aston et al. 2019), growth rate (Leichter and Genovese 2006) and feeding strategies of corals (Roder et al. 2010; Pacherres et al. 2013; Williams et al. 2018; Safaie et al. 2018; Radice et al. 2019). Besides affecting corals on a long-term scale, upwelling can also mitigate the effects of heat stress and create local refugees, as it can lower the water temperature (Schmidt et al. 2016; Reid et al. 2019; Wyatt et al. 2020; Storlazzi et al. 2020), and provide a new external source of nutrients to corals (Riegl et al. 2019). Moreover, high frequency temperature variability, often associated with internal waves-induce upwelling can increase the coral resistance to bleaching (Safaie et al. 2018). On the contrary, excessive nutrients can also exacerbate the effects of intense heat stress on reefs (Wiedenmann et al. 2013; DeCarlo et al. 2020; Burkepile et al. 2020). One way or another, upwelling affects coral reactions to bleaching events and should be studied thoroughly.

The work presented here aims at understanding upwelling dynamics linked with El Niño events in the central tropical Pacific. Such study could provide a better understanding of the mitigating effects of upwelling dynamics during El Niño, which could help define conservation-worthy locations for the future. Before any analysis could be made, a systematic way to detect and quantify upwelling dynamics must be used. Previous methods to quantify upwelling rely on a parameter-heavy methodology that requires an extensive knowledge of the local hydrography (Sevadjian et al. 2012; Gove et al. 2015; Williams et al. 2018). To complete our study, we first developed a new, automated and locally adapted-upwelling detection method that relies on a temperature stratification index. This is the focus of **Chapter I**. Once our method was developed, we applied it to ten years of subsurface temperature data in the U.S. unaffiliated territory of the Pacific Remote Island Area (PRIA) to understand upwelling dynamics in the area. The period extended from 2008 to 2017 and spanned two El Niño events: one in 2009 and a stronger one in 2015. We associated these temperature data with an El Niño index and 40 years of thermocline depth reanalysis to study interconnections between El Niño events, upwelling dynamics and thermocline depths. This is the matter of **Chapter II**.

Both chapters were written in collaboration with co-authors in order to be submitted to peer reviewed academic journals. Chapter I was written with Gareth J. Williams, J. A. Mattias Green (Bangor University), Jamison M. Gove (NOAA Fisheries) and Justin S. Rogers (Stanford University). In this chapter, I designed and developed the method with important feedback from all authors, while GJW, JAMG and I designed the study and wrote the manuscript. Chapter I has already been submitted to Limnology and Oceanography: Methods and we are waiting for the editors' comments. Chapter II is not yet in an appropriate format for submission but will be in the near future. Chapter II was written with

Gareth J. Williams and J.A. Mattias Green. In Chapter II, I conducted the analysis with feedback from GJW and JAMG while we all designed the study and wrote the manuscript.

I hereby declare that this thesis is the results of my own investigations, except where otherwise stated. All other sources are acknowledged by bibliographic references. This work has not previously been accepted in substance for any degree and is not being concurrently submitted in candidature for any degree unless, as agreed by the University, for approved dual awards.

Chapter II. Quantifying upwelling in tropical shallow waters: a novel method using a temperature stratification index.

II.1   Introduction

Temperature variations in the ocean can occur over years due to circulation changes (McPhaden 2015), over months due to seasonal differences in surface layer warming (Rao and Sivakumar 2000) and sub-daily due to temporary changes in the physical properties of the water column (Safaie et al. 2018). These latter short-term intrusions of cold water can affect a range of ecosystem patterns and processes. On tropical coral reefs, for example, short-duration upwelling events can redistribute larvae, plankton and nutrients throughout the water column (Pineda 1991; Leichter et al. 1996; Sevadjian et al. 2012), creating spatial disparities in resource supply that affect the growth rates of reef organisms (Leichter and Genovese 2006), their patterns of abundance (Aston et al. 2019), and their feeding ecology (Roder et al. 2010; Pacherres et al. 2013; Williams et al. 2018; Radice et al. 2019). Upwelling can also create temporary thermal refugia during abnormally high ocean temperature conditions (Reid et al. 2019; Wyatt et al. 2020) that can buffer the ecological impacts of mass coral bleaching and mortality (Wall et al. 2012; Schmidt et al. 2016; Safaie et al. 2018; Randall et al. 2020). Given these strong links between high-frequency temperature variations and the ecology of shallow-water tropical communities, we require a replicable method to quantify short-term cooling events.

Previous methods to quantify in situ cooling associated with upwelling from temperature time-series data consist of integrating all temperature values below a daily threshold, such as the daily mean (Leichter and Genovese 2006) or mode (i.e. most found temperature value in a day; e.g. Wall et al. (2012); Schmidt et al. (2016)). The resulting metric of degree cooling days is then simply a sum of all cooling times across the entire temperature time-series. A second method used by Wyatt et al. (2020) quantified cooling associated specifically with internal wave activity. Internal waves are sub-surface gravity waves that break and dissipate energy at depth and by doing so, drive deep cooler water up into the warmer shallows (Alford et al. 2015; Woodson 2018). By filtering the temperature time-series to retain all variability associated with frequencies between the local inertial frequency and the time-series sampling rate, Wyatt et al. (2020) identified cooling assumed to be linked to internal wave-induced upwelling. The aim of this method was not to quantify upwelling dynamics per se, but to quantify the overall temperature reprieve internal wave-induced upwelling affords shallow water reefs during thermal stress events.

However, the methods developed by Leichter and Genovese (2006) and Wyatt et al. (2020) have some limitations. Firstly, they give a summed value of high frequency temperature cooling across an entire time-series, but do not allow for the identification and timing of individual cold pulse events. Secondly, they do not identify the directional origin of the cold-water mass. Wyatt et al (2020) assumed that all high frequency temperature drops occurred as a result of deep-water internal waves. This is not always the case when cold surface water sinks down through the water column as a result of a thermally driven gravity current following cold, possibly nocturnal, atmospheric conditions (Monismith et al. 2006; Williams et al. 2018).

An automated method to identify individual cold pulses in temperature time-series data was first presented by Sevadjian et al. (2012) and, to date, has been the most widely adopted in tropical coral reefs studies (Gove et al. 2015; Williams et al. 2018; Aston et al. 2019; Comfort et al. 2019). The original method defines a cold pulse as whenever the temporal temperature gradient drops below a defined threshold (Sevadjian et al. 2012). If the temperature gradient stays below this threshold and the final temperature drop is greater than a specified value, a cold pulse is recorded. The event ends when the temperature recovers to a given fraction of its overall drop. There have been adaptations of the Sevadjian et al. (2012) method, including only identifying cold pulses with durations less than 13 hours to focus on cooling events associated with tidal and supertidal frequencies (Gove et al. 2015; Williams et al. 2018), as well as only those with a defined temperature drop occurring over a defined amount of time; the gradient then did not have to be maintained (Comfort et al. 2019). In Williams et al. (2018) and Comfort et al. (2019), the routine was applied to subsurface temperature recorders in a depth array at the same location. If the cold pulse was recorded in an upslope direction (i.e., recorded first in the deepest logger and then sequentially up into the shallows), it was attributed to upwelling induced by internal waves. However, if the reverse was seen and the cooling occurred first in the shallows and transitioned across the loggers in a downslope order, the cooling was attributed to surface downwelling (Williams et al. 2018).

In the following we will refer to the Sevadjian et al. (2012) method and its adaptations as the Constant Gradient Threshold (CGT) method, because the temperature gradient threshold for defining a cold pulse remains the same throughout the time-series. CGT methods are defined by four parameters: a gradient threshold, a minimum temperature drop, the overall temperature drop fraction that has to recover to mark the pulse end, and a maximum pulse duration. These parameters must be defined a priori, meaning cold pulse detection ultimately depends on these somewhat arbitrary parameter choices. For example, a cold pulse can be easily missed if it shows a final temperature drop smaller than the defined minimum temperature drop. The CGT methods also do not automatically detect the directional origin of each cooling event and these must be manually identified from the temperature records, making it a labour-intensive

process for isolating upwelling-induced cooling. It would therefore be beneficial to have a standardised way of defining the parameters based on the geographic location and time of the study, and an automated way to isolate and quantify cooling events related to upwelling. Here we present a new method that achieves this when applied to in situ temperature time-series data collected across depths in shallow and weakly stratified tropical waters, like those around coral reefs.

II.2 Materials and procedures
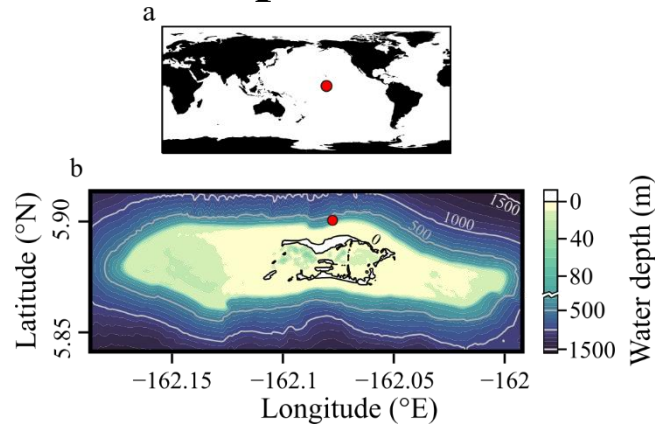
Figure II.1 Location of Palmyra Atoll in the central Pacific (a) and our study site on the north outer reef slope (b). Bathymetry data derived from multibeam bathymetry surveys collected by NOAA's Pacific Islands Benthic Habitat Mapping Center (up to 25 m) and IKONOS satellite data (shallower than 25 m). Solid lines represent the 0m, 500m, 1000m and 1500m bathymetry contour lines. The red circle represents the location of our test data set.

II.2.1 Data

For method development, we used temperature recorded over a year from April 17th 2015 to April 17th 2016 at three depths (6, 14, and 26 m) at a single location on the north outer reef slope (reef habitat facing the open ocean) of Palmyra Atoll in the Northern Line Islands, central Pacific (5°53'49''N - 162°04'41''W, see Figure II.1). Measurements were taken using Sea- Bird Electronics © sub-surface temperature recorders (SBE 56) attached to the reef floor and sampling every 5 min with an accuracy of 0.002°C. The data used were collected by the Ecosystem Sciences Division of the National Oceanic and Atmospheric Administration (NOAA) Pacific Island Fisheries Sciences Center's (PIFSC) Pacific Reef and Monitoring Program (RAMP).

II.2.2 Method

In weakly stratified tropical marine environments, near-surface stratification variability can be linked to the presence of a cool and dense internal tidal bore (Walter et al. 2012). An internal tidal bore is a gravity current formed by a breaking internal wave. The bore strength proxy, used in Walter et al. (2014) and based on a stratification index (Simpson and Pingree 1978), indicates the magnitude of an internal bore. The proxy is calculated as the difference between the potential energy of the water column if it was fully mixed and the potential energy of the observed water column divided by the height of the water column.

Physically, the bore strength proxy represents the energy required, per metre of depth, to fully mix the whole water column. Cold water intrusion, or cold pulses, in a weakly-stratified environment should therefore be detectable using a temperature proxy similar to the bore strength proxy.

In the following equations, depth averaged quantities are overlined ($^-$). The bore strength proxy for a water column at a time t, $\phi(t)$, is defined as (Walter et al. 2014):

$$\phi(t) = -\frac{g}{H} \int_{z_{max}}^{z_{min}} \left(\rho(z,t) - \bar{\rho}(t) \right) z dz \tag{1}$$

where $g = 9.81 \text{ m s}^{-2}$ is the gravitational acceleration, H the water column height, z_{max} and z_{min} the maximum and minimum depth of the water column, $\rho(z,t)$ the instantaneous density at a depth z and time t, and $\bar{\rho}(t)$ is the mean profile density. To detect cold-water intrusion in a water column, we adapt Eq. (1) to give a Temperature Stratification Index (TSI), ϕ_T, defined as:

$$\phi_T(t) = \frac{1}{H} \int_{z_{max}}^{z_{min}} \left(T(z,t) - \bar{T}(t) \right) z dz \tag{2}$$

Note Eqs. (1) and (2) are analogous and different only by a constant multiplier ($\phi \propto \phi_T$) if the density in Eq. (1) is primarily a function of temperature ($\rho \propto -T$), which is reasonable for shallow reef environments with few freshwater sources. In Eq. (2), T(z, t) is the temperature time-series of the vertical temperature structure and $\bar{T}(t)$ is the depth-averaged temperature time-series. If the temperature data are discrete over n equally spaced depth levels, $z_1, z_2, \ldots z_n$, Eq. (2) can be written, using a midpoint Riemann sum, as:

$$\phi_T(t) = \frac{1}{n} \sum_{i=1}^{n} \left(T(z_i, t) - \bar{T}(t) \right) z_i = \overline{\left(T(z,t) - \bar{T}(t) \right) z} \tag{3}$$

In the following, Eq. (3) is used for almost equally spaced data.
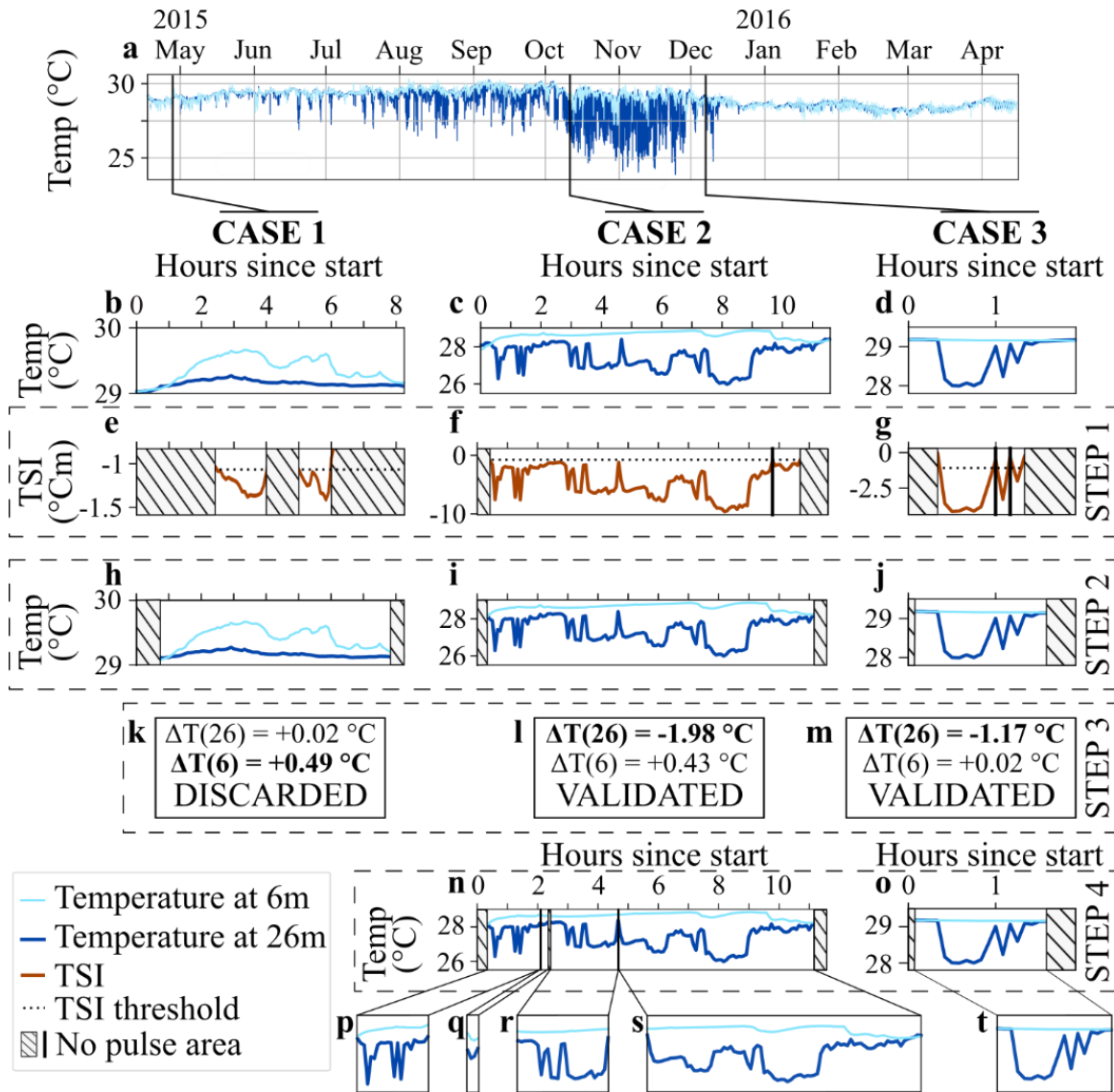
Figure II.2 Our automated detection of upwelling-induced cold pulses within subsurface temperature time-series data in shallow tropical environments using a temperature stratification index (TSI). The figure shows the step-by-step algorithm in three cases. CASE 1 (b, e, h, k) displays a potential pulse detected linked to heating in the surface layer and discarded by the algorithm. CASE 2 (c, f, i, l, n, p-s) displays a potential pulse detected containing a series of four successive cold pulses. CASE 3 (d, g, j, m, o, t) displays a potential pulse detected containing only one cold pulse. a-d. Input temperature data from the northern reef slope at Palmyra Atoll at 6m (light blue) and 26m (dark blue) depth. e-g. STEP 1: the TSI (thick solid red line) is computed from the input temperature data and potential pulses are defined as continuous periods of TSI lower than the location-specific threshold (thick dotted line). Hashed areas show where no potential pulse has been detected. h-j. STEP 2: boundaries of potential pulses detected are expanded to capture the full extent of the pulses. The figure shows the temperature data of the full potential pulses detected between the hashed areas. k-m. STEP 3: potential pulse linked to heating of the surface layer are discarded by the heating filter. The filter computes ΔT for each depth, defined as the difference between the pre-pulse temperature and the temperature of the minimum TSI. A pulse is discarded if ΔT at the deepest logger is positive, i.e. the bottom layer is warming, or if ΔT at the deepest logger does not have the biggest magnitude, i.e. a shallower layer experienced more temperature changes during the potential pulse. Computed ΔT for 6m and 26m are displayed. The ΔT with the biggest magnitudes are in bold. Potential pulse in CASE 1 is discarded, while potential pulses in CASE 2 and CASE 3 are validated. n-o. STEP 4: when potential pulses detected and validated by the heating filter contain several successive pulses, they are broken down into individual pulses. p-t. Individual cold pulse events detected by the algorithm.

15

The TSI is negative in a water column where the temperature is decreasing with depth. For a water column with a quasi-homogeneous temperature distribution, the TSI is close to zero. The TSI decreases as the temperature becomes more stratified as a result of cold-water intrusion at the bottom of the water column and the strength of the intrusion is quantified by the magnitude of the TSI. We calculate the TSI for temperature time-series data collected by loggers in a depth array at the same location. This allows us to quantify cooling events experienced by those loggers shallower than the logger in the array to which the TSI calculation is applied. The method is therefore restricted to data collected by two or more loggers in a vertical depth array at the same horizontal location.

In summary, our novel TSI method detects and quantifies upwelling-induced cold pulses in a warm, weakly stratified water column from a vertical array of temperature time-series data (Figure II.2). Note that this process only detects pulses at the deepest logger used in the array. The step-by-step process is as follows and we provide detailed descriptions of the methods behind each step below:

STEP 1 – Detecting potential cold pulses: for each time step, we compute the temperature stratification index (TSI) for the water column and extract potential cold pulses as being continuous periods of TSI below a location-specific threshold.

STEP 2 – Capturing the full extent of pulses detected: potential pulses detected only encapsulate the part of the pulses with the strongest stratification. We therefore expand the boundaries of those potential pulses to capture their whole extent.

STEP 3 – Filtering out potential pulses linked to surface heating: heating of the surface layer may also induce temperature stratification of the water column that can show up as a potential pulse. We therefore filter potential pulses linked to heating at the shallowest logger using a custom-made heating filter.

STEP 4 – Separating series of pulses: In the eventuality of several successive pulses detected, the event is broken down into individual pulses. Potential pulses remaining at that stage are considered true upwelling-induced cold pulses.

II.2.3   Detailed description of the method steps

II.2.3.1   Step 1: detecting potential cold pulses

An upwelling-induced cold pulse should first cause a sharp temperature drop at the deepest logger in the array before propagating up the reef slope to shallower depths. The lag between the temperature drops at different depths causes a noticeable temperature stratification captured by a negative TSI. A potential upwelling-induced cold pulse is defined as a continuous period of abnormally low TSI below a certain

threshold. To compute a locally relevant TSI threshold, we use in-depth monthly temperature data from the National Center for Environmental Prediction Global Ocean Data Assimilation System reanalysis product (NCEP/GODAS; Behringer and Xue (2004)), available from https://psl.noaa.gov/data/gridded/data.godas.html. GODAS temperature data are monthly means covering the whole globe from 1980 to 2020, with a spatial resolution of 0.333° latitude × 1° longitude, across 40 depth levels in 10-m increments from 5 to 225 m depth. From the GODAS data, we compute the location-specific climatological mean and standard deviation of the TSI. We first extract the temperature time-series from the GODAS data at the closest data point to our location (for our test dataset: 5°50'N - 162°30'W, 47 km away from our location). Then, the extracted data is interpolated to the depths of our subsurface temperature recorders and we compute the TSI time-series for our temperature time-series. We then use the TSI time-series to compute a 40-year climatological mean TSI and standard deviation, and define an abnormally low TSI as a TSI lower than the climatological mean minus one standard deviations. Our threshold, θ, is therefore defined as:

$$\theta = \overline{\phi_{T-GODAS}} - \sigma(\phi_{T-GODAS}) \tag{4}$$

In Eq. (4), $\overline{\phi_{T-GODAS}}$ is the 40-year climatological mean TSI and $\sigma(\phi_{T-GODAS})$ the 40-year climatological standard deviation. Using the threshold θ in Eq. (4), we can compute a list of the start and end times of potential cold pulses within the temperature time-series data.

II.2.3.2   Step 2: Capturing the full extent of pulses detected

The potential cold pulses detected only represent the part of the pulses where the TSI magnitude is the strongest. To capture the full extent of the pulses we define new boundaries in time for each potential pulse. For the new pulse start time, we first compute the last time step before the start of the potential pulse meeting one of three criteria (the TSI is increasing, the TSI is positive or the deepest logger temperature is not the minimum temperature in the water column). The new start is then defined as the time step right after the one we just computed. Similarly, for the new end time step, we compute the first time-step after the end of the potential pulse meeting one of two other criteria (the TSI is positive or the deepest temperature logger is the maximum temperature in the water column). The new end is then defined as the time step before the one we just computed. If potential pulses overlap, they are merged into a single potential cold pulse.

II.2.3.3   Step 3: Filtering out potential pulses linked to surface heating

Because the TSI is based on temperature differences between temperature loggers in a vertical depth array, a potential cold pulse may be recorded due to the water column surface heating instead of the bottom of the water column cooling. We therefore apply a heating filter to all potential pulses to remove those that are not linked to cooling at the deepest logger. This is done for each potential pulse by computing the

temperature difference between the start of the pulse and the time with the minimum TSI (i.e. the maximum TSI magnitude) for each depth. A pulse is authenticated under two conditions. First, the bottom temperature needs to be decreasing between the start of the potential pulse and the time of the minimum TSI. Second, the magnitude of the temperature difference needs to be greater for the bottom logger than for all the other loggers. If one of these conditions is not met, the potential pulse is discarded.

II.2.3.4   Step 4: Separating successive pulses

After the heating filter is applied, a detected pulse might in some cases actually be a series of successive individual cold pulses in close succession. To identify and separate these, we apply the following recursive routine, which we call the S-routine.
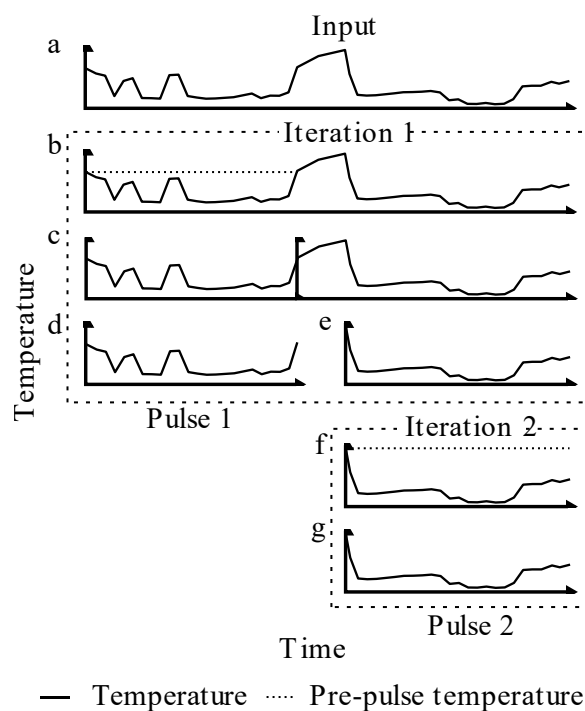
Figure II.3 Detailed schematic of our S-routine applied to a hypothetical series of cold pulses. Solid lines represent temperature data over time. Horizontal dotted lines are the pre-pulse temperature for each step of the routine. The potential pulse detected is split into two individual time-series after two iterations of the S-routine.

Initialisation: The pre-pulse temperature is defined as the temperature at the first time-step of the detected potential pulse (Figure II.3.a and II.3.f).

IF the temperature of the potential pulse remains below the pre-pulse temperature for the whole duration of the event (Figure II.3.f.)

- We categorise the potential pulse as an individual event (Figure II.3.g) and the S-routine ends.

ELSE (Figure II.3.b)

18

- The potential pulse is split in two parts (Figure II.3.c).
- We first categorise the part from the start to when the temperature goes back to the pre-pulse temperature as an individual cold pulse event (Figure II.3.d.).
- We then define the start a new potential pulse within the residual time-series. The new potential pulse starts when the bottom logger temperature decreases (Figure II.3.e).

IF no such time is found

- The potential pulse is categorised as nothing and the S-routine ends

ELSE

- We apply the S-routine to the new potential pulse (Figure II.3.f).

II.3 Assessment

To assess the performance of our temperature stratification index (TSI) against the previous constant gradient threshold (CGT) methods (Sevadjian et al. 2012; Gove et al. 2015), we first built a test data set by manually identifying cold pulses occurring at 26m depth in our Palmyra time-series data. From this data set, we extracted a list of indices, called 'real indices', from these test data, corresponding to the timestamps of the time series associated with the presence of a cold pulse. We then computed a list of indices for the presence of cold pulses as determined using the TSI and CGT methods applied to the original unprocessed time-series data, called 'predicted indices'. From there, we define precision, recall and F_1 score of each method, classically used for the assessment of anomaly detection algorithms (Anneken et al. 2015; Ji et al. 2019; Li et al. 2020), as in Eqs (5-7), where $\cap$ represent the intersection and | . | the size of a set of indices.

$$\text{Recall} = \frac{|(\text{Real indices}) \cap (\text{Predicted indices})|}{|\text{Real indices}|} \tag{5}$$

$$\text{Precision} = \frac{|(\text{Real indices}) \cap (\text{Predicted indices})|}{|\text{Predicted indices}|} \tag{6}$$

$$F_1 \text{ score} = 2\frac{\text{Precision} \times \text{Recall}}{\text{Precision} + \text{Recall}} \tag{7}$$

The higher the recall, the higher number of true positives, the higher the precision and the less false positives. The F_1 score is affected by both false negatives (as in recall) and false positives (as in precision). We consider both errors to matter equally in the process of detecting cold pulses, therefore we used the F_1 score as a proxy to rank the various detection methods against each other.

Our TSI method requires at least two temperature loggers (high accuracy and fast response time to changes in temperature, e.g. Sea Bird Electronics© SBE 56) to be used in a vertical array in order to compute the stratification in temperature across the loggers. To quantify upwelling at a certain depth, the TSI computed as in Eq. (3) is affected by the number of loggers used and their spatial organisation. To test for an effect of the number of loggers and their vertical depth spacing on the TSI values, we assessed the performance of our method in three different ways: first using all three loggers at 6, 14, and 26 m depth (called TSI(3) for TSI with three levels), then using the 26 m and the 6 m loggers (called TSI(2,20) for TSI with two levels, 20 meters apart), and finally using the 26 m and 14 m loggers (called TSI(2,10) for TSI with two levels, 10 meters apart). The TSI method achieved average precision of 92.6%, recall of 71.6% and F_1 score of 80.6% (Table 1). Precision was consistent across methods and varied from 91.5% to 93.1%. Recall varied more, ranging from 65.7% to 75.7%. The best F_1 score, i.e. the best of the three setups in our case, was obtained by the TSI(2, 20) (82.9%), closely followed by the TSI(3) (82.1%) and the TSI(2,10) (77%) (Figure II.4, Table II.1).

The CGT methods detect cold pulses based on the temporal temperature gradient: if the gradient exceeds a defined threshold (G, in °C min^{-1}), a potential pulse is recorded. If this potential pulse induces a temperature drop greater than a given minimum temperature drop (D, in °C), the potential pulse is considered to be a true cold pulse. The pulse event is considered over when the temperature has recovered to a defined fraction (F, no unit) of the induced temperature drop. If the pulse is longer than a given maximum duration (d, in hours), it is discarded. A given CGT method is thus defined by four parameters and will be referred as CGT(G: value of G, D: value of D, F:value of F, d: value of d). We first assessed the performance of the CGT methods used in Sevadjian et al. (2012) and Gove et al. (2015) corresponding to CGT(G:0.06, D:0.3, F:0.5, d: +∞) and CGT(G:0.00125, D:0.3, F:0.5, d:13), respectively. To compute the range in precision, recall and F_1 scores and thus the performance extent of the CGT methods, we varied all four parameters across reasonable ranges (Table 1). G logarithmically varied from 0.0008 °C min-1 (minimum detectable gradient using our loggers and sampling frequency) to 0.8 °C min-1 (near the maximum gradient found in the time-series: 0.89°C min-1) among 13 values, D varied from 0°C to 1.5°C every 0.1°C, F varied from 0 to 0.9 every 0.1, and d varied across three typical values (13h, 24h and 48h). The CGT methods examined showed a wide range in precision (0% to 100%) and recall (0 to 97.2%) (Figure II.4). The highest F_1 score of all CGT methods tested was 72.9%, obtained by the CGT(G:0.0008, D:0.1, F:0.9, d:24), corresponding to the lowest G, highest F and filtering pulses below 0.1°C (Table 1). The highest F_1 score of our TSI method applied to the test data was 82.9% and varied between 4.1-10.0% higher than the best F_1 scores achieved by the previously published CGT methods, regardless of the CGT method parameter settings (Figure II.4)
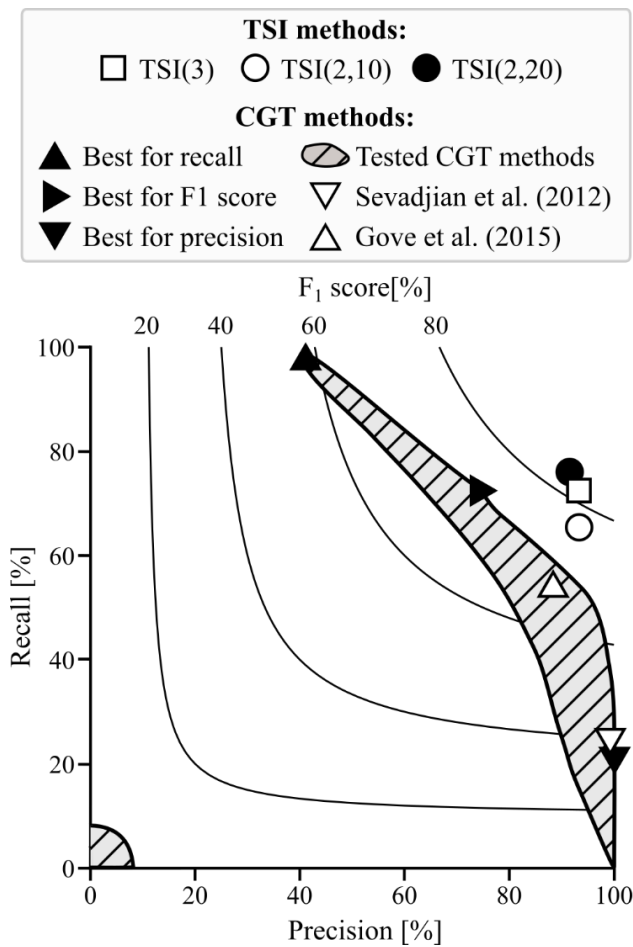
Figure II.4 Temperature stratification index (TSI) and constant gradient threshold (CGT) methods plotted on a precision-recall plane. Curved lines represent the F_1 score, increasing from the bottom left corner to the top right corner. TSI methods are represented by: a white square for the TSI(3), a white circle for the TSI(2,10) and a black circle for the TSI(2,20). All CGT methods are represented by the hatched area. White triangles represent previously published CGT methods (downwards for Sevadjian et al. (2012), upwards for Gove et al. (2015) while black triangles represent best CGT methods for a certain criterion (upwards for recall, rightwards for F_1 score and downwards for precision).

Table II.1 Precision, recall and F_1 score of important methods tested.

Method	Precision (%)	Recall (%)	F_1 score (%)
TSI[1](3)	**93.1**[2]	73.4	82.1
TSI(2,20)	91.5	**75.7**	**82.9**
TSI(2,10)	**93.1**	65.7	77.0
Mean TSI	92.6	71.6	80.6
Best CGT[3] for precision: CGT(G:0.025, D:0.9, F:0.3, d:24)	**100**	20.1	33.5
Best CGT for recall: CGT(G:0.0008, D:0, F:0, d:48)	42.0	**97.2**	58.6
Best CGT for F_1 score: CGT(G:0.0008, D:0.1, F:0.9, d:24)	73.8	72.1	**72.9**
Sevadjian et al. (2012): CGT(G:0.06, D:0.3, F:0.5, d(+inf))	99.5	18.1	30.6
Gove et al. (2015): CGT(G:0.00125, D:0.3, F:0.5, d:13)	88.9	52.2	65.8

[1] Temperature stratification index.

[2] Bold values represent the best scores reached by the TSI and the CGT methods in each column.

[3] Constant gradient threshold.

II.4 Discussion

Gradients in upwelling can have profound effects on the biology and ecology of shallow-water tropical marine communities (Leichter and Genovese 2006; Williams et al. 2018; Aston et al. 2019; Radice et al. 2019; Randall et al. 2020), yet we lack a locally parameterized automated method to quantify the dynamics of such events from in situ temperature timeseries data. Here we developed a novel method, the Temperature Stratification Index (TSI), that is parameterized based on the local temperature stratification of the water column to quantify sub-surface cooling events in highly stratified waters like those found around tropical coral reef islands. Based on in situ temperature timeseries data collected in a vertical depth array, our method improves on previously published methods by: 1) detecting individual cold pulse events to allow the computation of summary metrics, 2) removing the need for user-defined input parameters, 3)

automatically determining the directional origin of the cold-water mass to isolate cooling as a result of upwelling, and 4) increasing the detection accuracy (F_1 score) by up to 10%.

Previously published methods quantify integrated cooling across in situ temperature time series data (Leichter and Genovese 2006; Wall et al. 2012; Wyatt et al. 2020), but do not identify individual cooling events, preventing the calculation of summary metrics of cold pulse temporal dynamics. In contrast and like previously published constant gradient threshold (CGT) methods (Sevadjian et al. 2012; Gove et al. 2015), our TSI method detects individual cold pulse events, allowing metrics such as mean pulse duration, mean maximum temperature drop, and mean pulse frequency to be calculated over different temporal windows. Depending on the question at hand, these metrics could be critical. For example, around both continental and oceanic shallow-water tropical coral reefs, cold pulses as a result of deep-water upwelling are associated with increased nutrient supply to the shallows (Leichter et al. 2003; Aston et al. 2019). Cold pulses with a mean short duration could favour macroalgae that are able to capitalise on increased nutrient concentrations in the surrounding waters more rapidly than reef-building corals (Fujita 1985; Raven and Taylor 2003; Ladah et al. 2012; Den Haan et al. 2016). In contrast, reef-building corals may benefit where cold pulses occur more frequently or have a longer mean duration. In the central Pacific, the percentage cover of reef-building corals around Jarvis Island peaked where more frequent deep-water cold pulses occurred (Aston et al. 2019), and mean duration of cold pulses associated with night time lagoonal flushing correlated more strongly with coral trophic responses than the total cooling time of these events around Palmyra Atoll (Williams et al. 2018). These ecological responses to specific cold pulse dynamics would be missed by purely quantifying the summed total amount of cooling over time.

A cold pulse identification method that requires a priori defined input parameters runs the risk of the user making arbitrary choices or them taking parameter values from previous studies conducted under different environmental contexts. The CGT method used by Sevadjian et al. (2012) and Gove et al. (2015) requires four input parameters to be defined by the user, but our TSI method does not require any pre-defined input parameters to identify individual cooling events within a temperature timeseries. Our method defines a 'cold pulse' in a geographically context-specific manner without the need for prior knowledge of the hydrographic properties of the study site. We define a cold pulse as a continuous period of "abnormally low" temperature stratification in the water column, with this criterion based on a climatological threshold of the temperature profile at the study site calculated from the NCEP-GODAS reanalysis product (Behringer and Xue 2004). The TSI cold pulse detection threshold is therefore automatically tuned for the study site in question, removing biases associated with user-defined input parameter choices.

In weakly stratified tropical waters, cold pulses can occur in temperature timeseries data as a result of surface downwelling in addition to deep-water, internal wave-driven upwelling (Williams et al. 2018). Despite both mechanisms creating short-term drops in sub-surface temperature, the cold-water masses driving the cooling response have fundamentally different origins and may therefore have different effects on shallow-water tropical organisms. Previously, the only way to separate cooling as a result of these different physical mechanisms was the labour-intensive process of manually inspecting each cold pulse identified by the CGT algorithm (Gove et al. 2015; Williams et al. 2018). The TSI method improves on this by automatically separating upwelling from downwelling-induced cooling events by investigating the sign of the temperature gradient. Upwelling-induced cold pulses result in a negative TSI, whereas cold pulses as a result of downwelling result in a positive TSI and are automatically discarded.

As well as solving the core limitations of previously published methods that quantify upwelling-induced cold pulses, our TSI method shows a substantially increased detection accuracy. Around the shallow tropical waters of Palmyra Atoll, our TSI method (and its variations tested in terms of number and spacing of loggers in a vertical array) achieved an F_1 score 4.1-10% better than the best CGT method, even with the CGT parameters optimised for the test data set (Table II.1, Figure II.3). The TSI method showing the best results was the method using TSI over two depth levels, 20 meters apart, with an overall F_1 score of 82.9% (10% higher than that of the best F_1 CGT score). If two loggers are available, we would advise users to choose the TSI method over any CGT method. Of course, the quality of the loggers is required to be of sufficient quality for either method. We advise users to utilise loggers with a high accuracy and fast response time to changes in temperature, such as the ones used here. Note that some loggers may be advertised as having high accuracy, but their response time to changes in temperature is slow and short duration cold pulse events may then be missed. The depth of logger placement should be chosen with care when using our TSI method as results can be affected by the local stratification. For example, if two loggers are too far apart or too deep, one logger could reside in the isothermal layer but not the other. In this case, the background stratification will be high and only the strongest upwelling-induced cold-pulse events may be detected. Similar underestimates are likely to be obtained in a region subject to constant intense upwelling, for example on the west coast of Jarvis Island that experiences high upwelling intensity and frequency induced by the Equatorial Undercurrent (Gove et al. 2006; Aston et al. 2019). Similarly, loggers too shallow will be affected by the daily temperature cycle in the atmosphere, which can bias the results, as pulses producing a smaller temperature difference than the one induced by the warm surface temperature are likely to be discarded during our heating filter processing step. Finally, if the two loggers are too close to each other, the temperature difference during a pulse might not be sufficient to create enough stratification for the event to be detected. With this in mind, we would advise future users who

want to detect cold pulses at a depth d to follow these recommendations (note that the depth of detection d corresponds to the depth of the deepest logger): 1) both loggers should sit in the isothermal layer and thus above the thermocline for the duration of the study, 2) the shallow logger should not be shallower than 5-10 m to limit the effects of air temperature on the underlying water mass, and 3) the shallowest logger should be at least 5-10 m above the deep logger to create a sufficiently large temperature difference during cold pulse events. The current work tested these methods with temperature data only as is commonly available. But if salinity data was available in addition to temperature data, the same methods outlined here could be extended to the density as in Eq. (1), a topic that could be investigated in future work.

In summary, upwelling has several effects on shallow-water tropical communities, but our ability to study these patterns and processes is dependent on our ability to quantify upwelling dynamics in a repeatable and rigorous manner. Our novel TSI method presented here improves on previously published methods by identifying individual cooling events within a temperature timeseries to allow the calculation of summary metrics associated with their dynamics without the need for user-defined input parameters. This means our method is easily applied to novel situations to quantify the dynamics of upwelling-induced cooling where previous hydrographic knowledge of the study site is lacking.

Chapter III. Temporary redistribution of upwelling-exposed areas in the tropical Pacific during El Niño

III.1 Introduction

Coral reefs are highly sensitive to local water conditions. Disruptions in the usual physicochemical properties, such as oxygen concentration (Altieri et al. 2017), acidity (Hoegh-Guldberg et al. 2007; Manzello 2010) or temperature (Hoegh-Guldberg 1999; Hughes et al. 2017) can have dramatic effects on corals. Under anomalously high temperature conditions, the algal endosymbionts of corals produce toxic reactive oxygen species and are expelled by their host, leading to coral bleaching (Hughes et al. 2017, 2018). Under normal conditions, the endosymbiont would provide food to the corals through photosynthesis, but bleaching leaves corals with no internal source of nutrition. If the heat stress perdures, the starvation induced by the bleaching can lead to mortality among corals (Glynn 1984; Vargas-Ángel et al. 2011; Furby et al. 2017; Sakai et al. 2019). In a changing climate, ocean warming is arguably the biggest threat to tropical reef environments, which is why the understanding of mitigating physical factors is vital for the future of reef conservation strategies.

In the tropical ocean, the thermocline separates a warm, nutrient-depleted surface layer from a warmer and nutrient-enriched deep water. Upwelling is a physical process that can bring sub-thermocline water up to the shallows (Ross and Sharples 2007). It can be generated by a current below the thermocline, like the Equatorial Undercurrent, which can be topographically steered up into the shallows (Gove et al. 2006), or by internal gravity waves, propagating on or below the thermocline and shoaling when they encounter bathymetry (Walter et al. 2012; Sutherland et al. 2013; Woodson 2018). A shallower thermocline would theoretically reduce the distance internal waves must travel before reaching shallow waters, eventually increasing upwelling intensity, assuming the strength of the stratification does not change. The delivery of sub-thermocline water to the surface layer through upwelling can have profound effects on nearshore ecosystems, and noticeably on coral reefs. It can create spatial disparities in the distribution of reef organisms (Aston et al. 2019), their growth rate (Leichter and Genovese 2006), or in the feeding strategy of corals (Roder et al. 2010; Pacherres et al. 2013; Williams et al. 2018; Safaie et al. 2018; Radice et al. 2019) through the creation of local cool and nutrient-enriched environments (Pineda 1991; Buerger et al. 2015; Safaie et al. 2018; Reid et al. 2019). High frequency temperature changes can also reduce coral susceptibility to bleaching (Buerger et al. 2015; Safaie et al. 2018). During periods of

intense heat stress, upwelling can therefore mitigate or exacerbate the intensity of coral bleaching by creating thermal refugia (Reid et al. 2019; Wyatt et al. 2020; Storlazzi et al. 2020), limiting the effects of the heat stress (Riegl et al. 2019). Because of the associated nutrient delivery, upwelling can also limit the mortality of corals and improve their recovery (Riegl et al. 2019), as long as it does not provide an excessive nutrient supply that can aggravate bleaching intensity and duration (Wiedenmann et al. 2013; DeCarlo et al. 2020; Burkepile et al. 2020). Upwelling is obviously a key process in the understanding of coral bleaching and mortality dynamics during heat stress.

The El Niño Southern Oscillation (ENSO) is a multi-year climate mode deeply affecting the global climate in terms of wind, precipitations, ocean currents and surface temperature (Zhang and McPhaden 2006; McPhaden et al. 2011). Mostly affecting the Indo-Pacific basin, ENSO oscillates between a warm El Niño phase and a cooler La Niña phase (Trenberth 1997). In the tropical Pacific, El Niño events are responsible for intense heatwaves affecting nearshore ecosystems. Since 1980, three El Niño of very strong magnitude triggered the most extensive bleaching and mortality events on record in the tropics: in 1982 (Glynn 1984), 1997 (Williams et al. 2010; Vargas-Ángel et al. 2011; Furby et al. 2017; Donner et al. 2017) and in 2015 (Hughes et al. 2017; Fox et al. 2019; Vargas-Ángel et al. 2019). Upwelling dynamics during the El Niño phase could potentially condition a reef's capacity to overcome intense heat stress by delivering cold, nutrient rich, water to the surface layer, but a quantification of this is missing in the literature.

Thermocline depth variability in the tropical Pacific is widely associated to ENSO at a basin-wide scale (Xu et al. 2017; Yang et al. 2019). During El Niño events, the tropical Eastern Pacific thermocline deepens while it shoals on the Western Pacific. Inversely, during the colder La Niña phase of the cycle, the thermocline shoals to the East and deepens to the West (McPhaden 2015). On a local scale, El Niño can also modulate upwelling variability in the Pacific as in the Galapagos (Riegl et al. 2019), Vietnam (Kuo et al. 2004), Chile (Montecinos and Gomez 2010) or Peru (Espinoza-Morriberón et al. 2017), often linked with thermocline variability. Those studies were conducted on upwelling-exposed areas, but the thermocline variations induced by El Niño could potentially generate new upwelling areas.

Palmyra Atoll is part of the U.S. territory of the Pacific Remote Islands Area (PRIA) and is a rich tropical coral reef removed from anthropogenic influence (Figures II.1, III.1). This makes Palmyra an ideal location on which to study processes at a pristine coral reef (Williams et al. 2010; Gove et al. 2015, 2016; Fox et al. 2018). Despite an intense heat stress during the 2015 El Niño, and an island-wide bleaching event affecting more than 90% of the corals, Palmyra showed limited mortality and high post-bleaching

recovery (Fox et al. 2019). However, the mechanism that saved Palmyra is not obvious, but strong upwelling is a prime candidate.

Here, we investigate interconnections between upwelling variability, thermocline depth and El Niño events at five locations in the PRIA. This is done by using ten years of subsurface temperature data from Palmyra Atoll provided by the National Oceanic and Atmospheric Administration (NOAA), a recently developed automated method to quantify upwelling dynamics (Guillaume-Castel et al. subm.) and a thermocline depth reanalysis product (Behringer and Xue 2004). We provide evidence that Palmyra was the set of an extreme upwelling event in 2015, which could have provided its corals with thermal shelter and food supply during the El Niño-induced heat stress. Moreover, we show that such events are a feature of strong and very strong El Niño events, and that all the studied islands were affected.

III.2 Materials and methods

III.2.1 Study site

The PRIA is an unaffiliated U.S. territory in the central tropical Pacific Ocean. Because of their distance from human habitation, the PRIA is ideal to study coral reef environments without anthropogenic factors, including disturbances such as flushed nutrients, fisheries or tourism. Of the seven locations in the PRIA, we will focus on five: Palmyra Atoll, Kingman Reef, and Howland, Baker and Jarvis islands (Figure III.1.a; we hereafter refer to them all as islands). Three distinct groups can be created, with Palmyra and Kingman 67 km apart just north of the equator (Figure III.1.c), Howland and Baker 70 km apart on the equator and to the west of Palmyra and Kingman (Figure III.1.b), and finally Jarvis on its own at the equator, 800 km south of Palmyra and 1800 km West of Howland and Baker (Figure III.1.d).
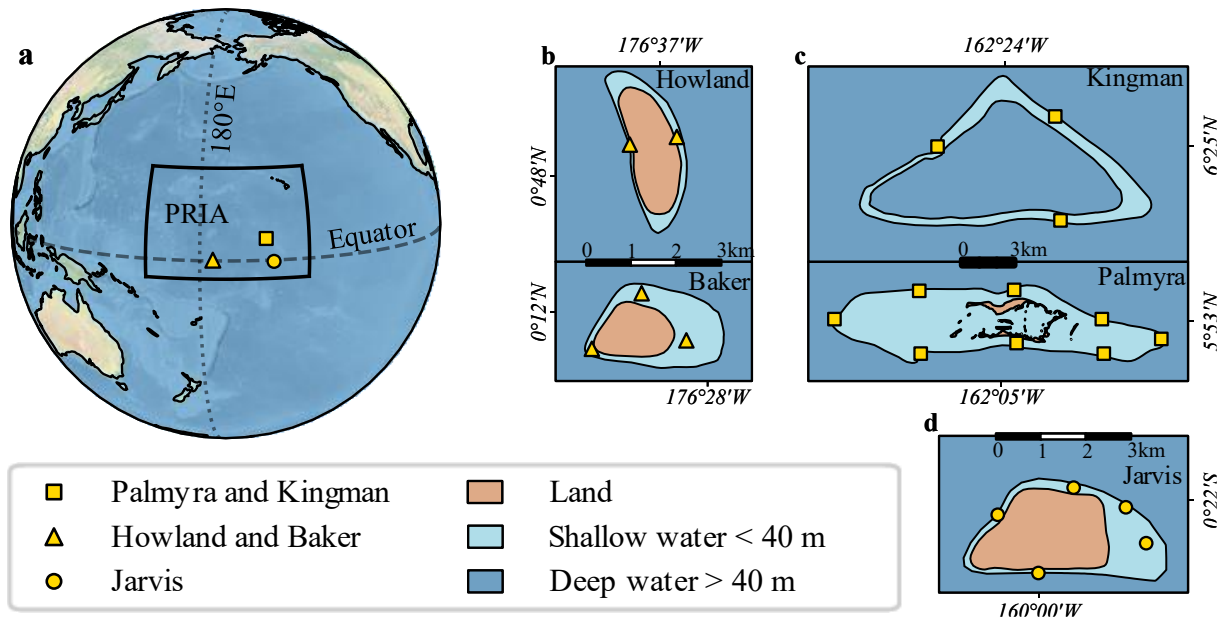
Figure III.1(a) Location of the Pacific Remote Island Areas (PRIA) in the Pacific Ocean, with specific locations for Palmyra and Kingman (square), Howland and Baker (triangle) and Jarvis (circle). The Equator is represented by the dashed line while the 180°E Meridian is the dotted line. **(b)** Schematic representation of Howland and Baker Islands and the locations of the loggers used in the study. **(c)** Schematic representation of Kingman Reef and Palmyra Atoll and the locations of the loggers used in the study. **(d)** Schematic representation of Jarvis Islands and the location of the loggers used in the study. In b-d, land is shown in beige, shallow water in light blue and deep water in blue. Panels b-d are adapted from (Miller et al. 2008), Figure 11.2 using Google Maps (https://maps.google.fr/maps).

III.2.2 Subsurface temperature data

We use ten years of in-situ subsurface temperature recorded by the Ecosystem Science Division of the National Oceanic and Atmospheric Administration (NOAA) Pacific Island Fisheries Sciences Center's (PIFSC) Pacific Reef and Monitoring Program (RAMP). The data studied span the years 2008 to 2017, and 2 to 8 study sites per location (Figure III.1.b-d). The subsurface temperature was recorded using Sea Bird Electronics© SBE37 and SBE56 loggers (henceforth referred to as STRs), with an accuracy of $\pm$ 0.002°C, and sampling frequencies ranging from 30s to 60min. Full details on loggers are presented in the Table S1.

III.2.3 Quantifying upwelling variability.

To quantify upwelling dynamics, we used the recently developed temperature stratification index (TSI) method (Guillaume-Castel et al. subm.). The TSI method is an automatic algorithm to detect upwelling-induced cooling events, or cold pulses, in temperature time series. Using two or more temperature loggers, the method uses the temperature stratification to compute a TSI. An upwelling-induced cold pulse is defined as a continuous period of abnormally low TSI, with criteria based on the local stratification climatology derived from NCEP/GODAS temperature data (Behringer and Xue 2004). The TSI method is therefore automatically tuned to the study location. When more than two simultaneous loggers were

available in an array of depths, we detected cold pulses for all depths but the shallowest one. The TSI was then applied to the logger at the given depth and the shallowest logger. For example, if three loggers are available, at 5m, 15m and 25m deep, we detected cold pulses at 15m using the 5m and 15m loggers, and at 25m using the 5m and 25m loggers. Distribution of the depths and locations were cold pulses could be detected are presented in Figure III.1.b-d and Figure III.2. Once we had detected the cold pulses, we computed instantaneous degree cooling weeks (DCW) (e.g., Gove et al. (2015); Williams et al. (2018)) as the difference between the pre-pulse temperature and the temperature during the pulse, multiplied by the time step of the time series in weeks. Instantaneous DCW are zero outside of cold pulse events. From there, we derived DCW, as the cumulative instantaneous DCW in the past 12 weeks.
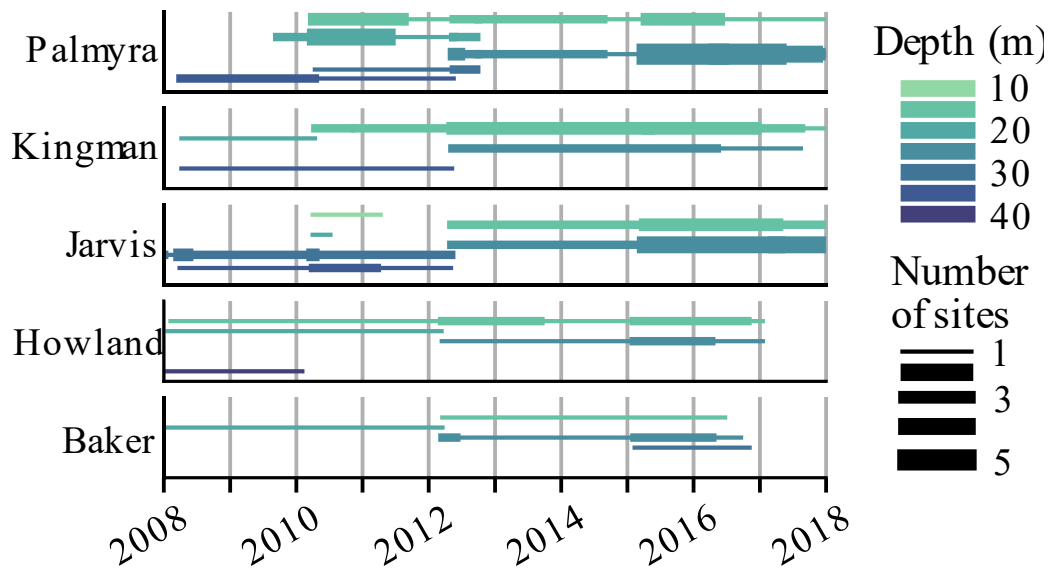
Figure III.2 Number of available locations where degree cooling weeks (DCW) are computable - i.e. with at least one simultaneous shallower logger is available at the same site – for each island and depth of the study. The position of the solid lines and their colour represent the depth while their width represents the number of sites where DCW can be computed at the corresponding depth.

III.2.4   El Niño Southern Oscillation data

The ENSO phase, used to characterise El Nino or La Nina years, was determined using the Oceanic Nino Index (ONI; https://ggweather.com/enso/oni.htm). ONI is a three-month rolling mean sea surface temperature (SST) anomaly over the Nino 3.4 region in the central Pacific (120°W to 170°W and 5°S to 5°N). El Niño (La Niña) events are defined when the ONI is continuously greater (less) then 0.5°C (-0.5°C). These events are characterised as weak if the SST anomaly does not exceed 1°C, moderate if the SST anomaly ranges from 1 to 1.5°C, strong if the SST anomaly is between 1.5°C--2°C, and very strong when the SST anomaly is greater than 2°C. Here, we will only consider moderate to very strong events; see Table II.1 for a summary.

Table III.1 Years associated with moderate to very strong El Niño and La Niña events since 1980 based on the Oceanic Niño Index.

Magnitude	El Niño years	La Niña years
Very strong	1982; 1997; 2015	None
Strong	1987; 1991; 2009	1988; 1998; 1999; 2007; 2010
Moderate	1994; 2002	1995; 2011

III.2.5   Thermocline depth data

We use thermocline depth data from the National Center for Environmental Prediction Global Ocean Data Assimilation System product (NCEP/GODAS; Behringer and Xue (2004)). GODAS is a global reanalysis product providing monthly averaged data from 1980 to the present day at a spatial resolution of 1/3° latitude × 1° longitude. The thermocline depth data from GODAS is computed as the depth where the temperature deviation from the surface temperature exceeds 0.8°C (see https://psl.noaa.gov/data/gridded/data.godas.html). When comparing thermocline depth and DCW, the former is the mean thermocline depth over the past three months, so it matches the averaging period of the DCW. When comparing thermocline depth to ENSO phases, we computed a mean bi-yearly thermocline depth profile by averaging month-by-month all years and their following corresponding to a given ENSO phase and magnitude. For example, the very strong Niño thermocline depth is computed by averaging the years 1982-1983, 1997-1998 and 2015-2016 (*cf.* Table II.1).

III.3   Results

III.3.1   Upwelling and thermocline depth variability linked to ENSO phases
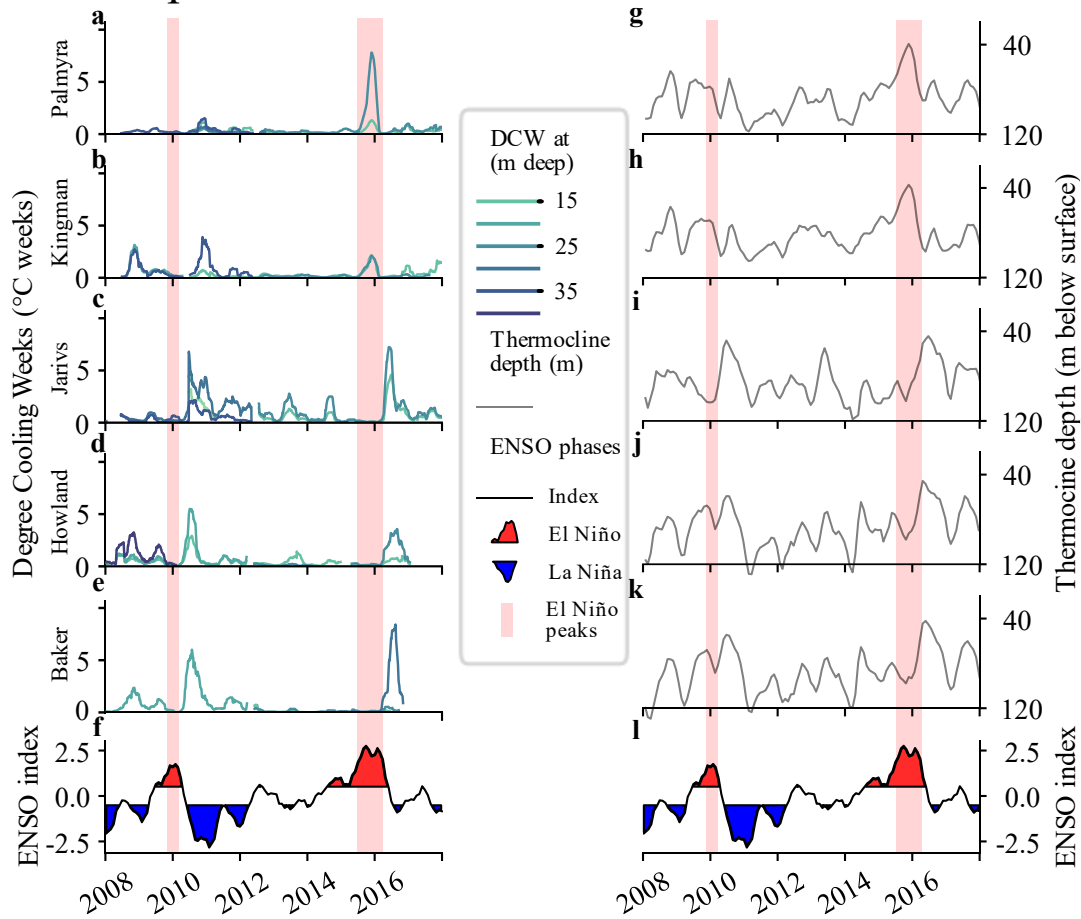
Figure III.3 Island-mean degree cooling weeks (DCW, a-e) and NCEP-GODAS three-months rolling thermocline depth (g-k) at Palmyra (a; g), Kingman (b; h), Jarvis (c; i), Howland (d; j) and Baker (e; k) along with ENSO phases (f; l) from 2008 to 2017. DCW are represented by the solid lines in shades of blue, where the brightness of the line represents the depth at which DCW were recorded (darker is deeper). Thermocline depths are represented by the solid grey lines. In (f; l), El Niño (La Niña) events are represented by red (blue) patches. The pink rectangles highlight the peaks of the 2009 and 2015 El Niño events.

We can observe variability in the response of thermocline depth and upwelling intensity facing El Niño events (Figure III.3). During the peak of the 2009 event, the upwelling was almost stopped and never exceeded 0.5 °C weeks at all locations. However, in 2010, Howland, Jarvis, and Baker experienced strong upwelling, peaking mid-year and lasting for six months, coinciding with the La Niña event. The DCW reached maxima of 6°C weeks at Howland and Baker (at 20 m depth) and 7°C weeks at Jarvis (at 35 m depth); note that all depths where we had STRs at that time were affected by the event. During the peak of El Niño in late 2015, a second intense upwelling event affected Palmyra and Kingman, again observed at all available depths. During this event, DCW reached 2°C weeks at Kingman and 7.5°C weeks at Palmyra (both at 25m deep). Similarly to the 2010 intense DCW period, another extreme upwelling event affected

Jarvis, Howland and Baker in mid-2016, with DCW reaching 7°C weeks at Jarvis (at 25 m), 3.5°C weeks at Howland (also at 25m) and 8°C weeks at Baker (at 35 m depth). This event matches the return to a La Niña phase. All the observed events are associated with a shallow thermocline at each of the affected islands (Figure III.3.g-k). At Palmyra and Kingman, the shallowest thermocline is detected in late 2015, reaching 40 m, more than 10 m shallower than the second lowest value (Figure III.3. g-h). At Jarvis, the two upwelling events detected correspond to thermoclines shallower than 50 m, whereas normally the thermocline rarely shoals above 80 m (Figure III.3.i). Finally, at Howland and Baker, the two upwelling events correspond to the two shallowest thermocline values at around 50m deep in 2010 and 60m deep in 2009 (Figure III.3.j-k).
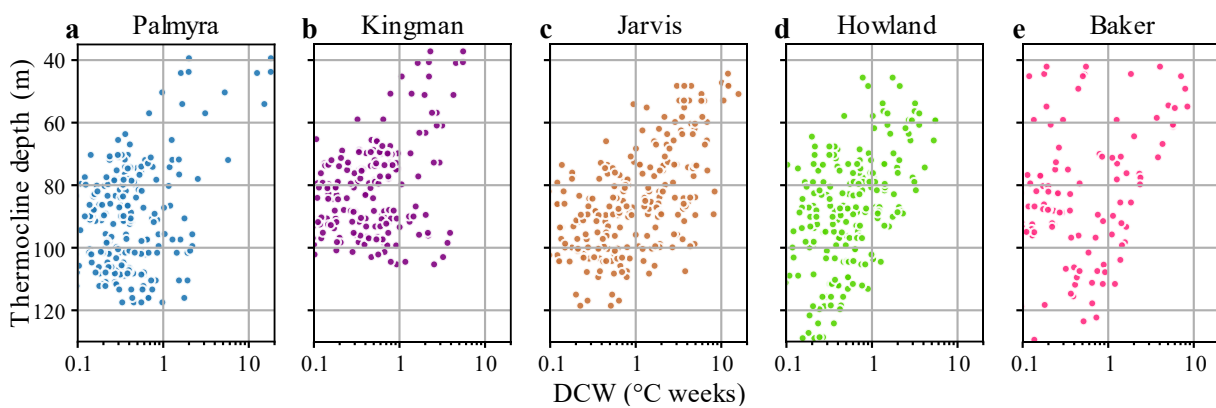
Figure III.4 DCW and three-months rolling thermocline depth at Palmyra (a), Kingman (b), Jarvis (c), Howland (d) and Baker (e) from 2008 to 2017. Each dot represents the DCW of one site and depth associated with the island thermocline depth. DCW are in log scale for better visibility.

At all islands, more upwelling, quantified through an increase in the DCW, is associated with a shoaling thermocline. At Palmyra, Kingman, Jarvis, and Howland, when the thermocline reached above 70-80 m depth, the DCW exceeded 0.1 °C weeks and often surpassed, 1 °C week above 60 m (Figure III.4. a-d). However, Baker still displays low DCW associated with a shallow thermocline. Furthermore, a high number of DCW were found for a deep thermocline at Kingman and Jarvis, but the strongest DCW remain present when the thermocline is shallow. Overall, these results indicate that strong upwelling can happen at various thermocline depths, although shallow thermocline are almost always associated with intensified upwelling at our locations. Similarly, deep thermocline at all locations but Kingman show limited upwelling when the thermocline is deep. Below 100m-110m, DCW rarely exceeded 2°C weeks.

III.3.2   Thermocline shoaling and magnitude of ENSO events

We refer the reader to Figure III.5 for the following discussion. Our five islands experience different thermocline shoaling signals during the ENSO phases. Palmyra and Kingman (Figure III. 5. a) experience a drastic thermocline shoaling during very strong El Niño years (i.e., 1982, 1997, 2015). The thermocline

reaches its shallowest depth between January to October in the El Niño years, when it shoals to 40 m depth, while the climatologically shallowest month is only slightly above 80m. Moderate and strong El Niño events also induce thermocline shoaling around these islands, but the shallowest depths are only 70 m. La Niña only induces deepening of the thermocline, from 80 m to 100 m at the islands.
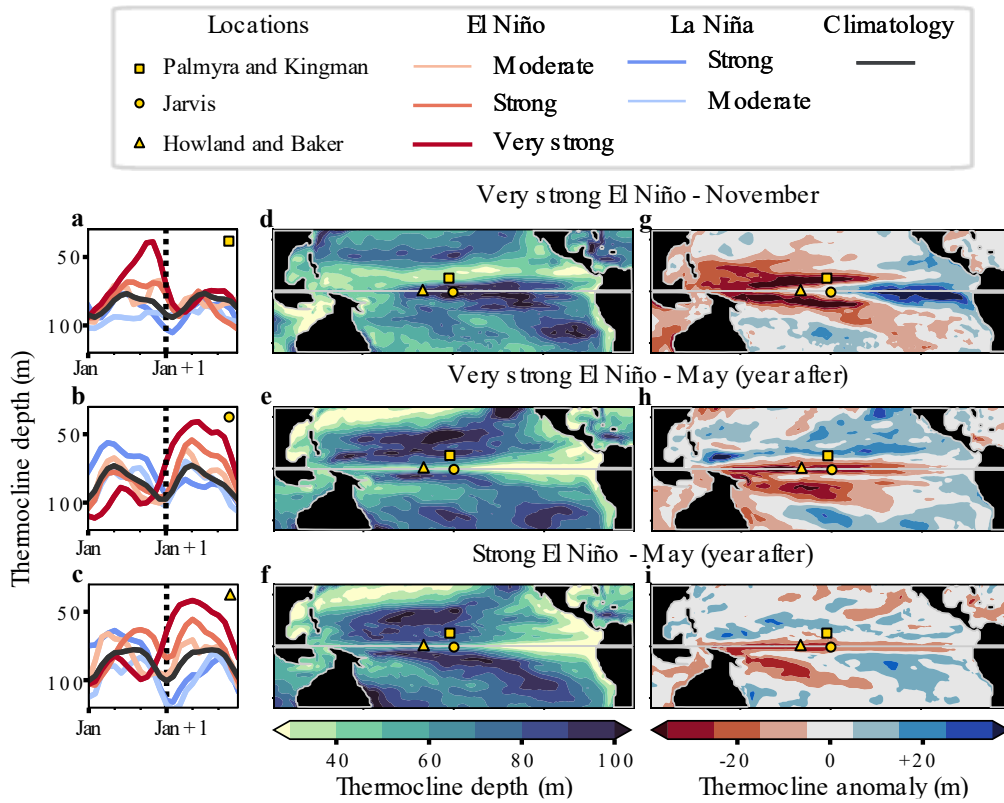
Figure III.5 (a-c) Mean three-months rolling NCEP-GODAS thermocline depth corresponding to different magnitudes of El Niño and La Niña events. Red (Blue) lines represent El Niño (La Niña) events at Palmyra and Kingman (a), Jarvis (b) and Howland and Baker (e). The darker and thicker the line, the stronger the magnitude, going from moderate to very strong for El Niño and from moderate to strong for La Niña. The monthly climatology is represented by the solid black line. **(d-i)** NCEP-GODAS three-months rolling mean thermocline depth (d-f) and thermocline depth anomaly (g-i) for three shoaling periods. The location of the island studied are represented by yellow markers: square for Palmyra and Kingman, circle for Jarvis and triangle for Howland and Baker. (d; g) show the thermocline depth and anomaly corresponding to November during all very strong Niño events since 1980. (e; h) show thermocline depth and anomaly corresponding to May the year after very strong Niño events. (f; i) show the thermocline depth and anomaly corresponding to May the year after strong Niño events. In g-i, shallower thermoclines than usual are represented by negative values (red shades) and deeper thermoclines by positive values (blue shades). Anomalies are defined using the monthly climatology as a baseline. The horizontal grey lines represent the Equator.

Very strong El Niño events affect Jarvis, Howland and Baker (Figure III.5.b-c) in a similar way. During the El Niño years, the thermocline is similar to or deeper than in the climatology, but the shoaling gradually starts in September until it reaches its minimum depth of 45-50 m between March and June the year after. Strong El Niño years experience a shoaling of the thermocline the year after the events at Jarvis, Howland and Baker, reaching depths shallower than 60 m. To a lesser extent, Howland and Baker also have a shoaling thermocline in the year of strong Niño events, but it remains 5 m deeper than

the year after the event. At Jarvis, a strong La Niña induce shoaling of the thermocline in the year of the event, lasting for the whole year and peaking at a depth of 60 m. The thermocline also shoals at Howland and Baker but only up to 70 m at the beginning of the year of the event.

El Niño events of strong and very strong magnitude are linked with regional thermocline shoaling patterns in the central tropical Pacific. At Palmyra and Kingman, very strong Niño events (1982, 1997 and 2015) triggered an intense shoaling of the thermocline, reaching three-months rolling means of 40m deep in November, 40m shallower than the shallowest monthly climatology. Similarly, La Niña phases following both strong and very strong Niño induced shoaling of the thermocline at Jarvis, Howland and Baker. The shoaling peaked in March (Howland), May (Baker) and June (Jarvis) reaching between 40 and 45m deep, 30m to 40m shallower than the shallowest monthly climatology of 70m at Jarvis and 80m at Howland and Baker. These events are not only limited to the central tropical Pacific but is basin-wide (Figure III.5.d-i). The shoaling during very strong Niño events affecting Palmyra and Kingman displays a 90° rotated V-shape (Figure III.5.g) pointing towards the West. The northern part of this V-shape allows the thermocline to reach depth of 40m in a diagonal line extending from the North tip of Australia to central America (Figure III.5.d). Both Palmyra and Kingman are in this northern part. The shoaling affecting Jarvis, Howland and Baker also extends across the whole Pacific, but more centred over the equator (Figure III.5.e-f; h-i) where the Western pacific equatorial thermocline reaches 40m after very strong Niño and 50m after strong Niño events.

III.4   Discussion

In 2015 the reefs at the atoll of Palmyra survived despite intense heat stress and a serious bleaching event (Fox et al. 2019), and the reason for the survival of the reef at Palmyra is not clear. We provide evidence supporting that Palmyra corals could have been saved by a strong, island-wide upwelling event directly linked to El Niño. Moreover, we suggest that these kinds of strong upwelling events are a feature of strong and very strong El Niño events in the central Pacific, and could affect wide geographical areas as in the region 1) strong and very strong El Niño induce thermocline shoaling patterns, and 2) shallow thermocline is linked to intensified upwelling.

III.4.1   Circumstances inducing the survival of Palmyra corals in 2015

Upwelling can provide shelter to coral reefs in times of heat stress through heat relief (Riegl et al. 2019), high frequency temperature variability (Safaie et al. 2018) or nutrients supply (Riegl et al. 2019). It can also improve post bleaching recovery (Riegl et al. 2019). According to Fox et al. (2019), degree heating weeks (DHW), a metrics to quantify heat stress on corals, showed a maximum of 12 °C weeks, widely

exceeding the 8°C weeks threshold causing coral mortality. They observed an intense bleaching event affecting more than 90% of the organisms at the atoll, but low mortality, contrasting with the intense heat stress. An external phenomenon was necessary for the corals to survive through this event, and upwelling was a perfect candidate. During the warmest period of the 2015-2016 El Niño (August to December), high frequency upwelling increased up to 7.5°C weeks, 13 times more than the ten-year mean intensity at 0.57°C weeks. Through its properties described earlier, upwelling could have both prevented Palmyra corals from dying and improved post-bleaching recovery.

However, there is no consensus on the intensity of the heat stress that affected Palmyra during the 2015-2016 El Niño. DHW are the most widely used heat stress metrics in coral reef studies. They are computed using a certain temperature threshold above which corals are expected to be affected by the heat. This threshold is usually computed as the maximum monthly mean (MMM) from the climatology. From the MMM, daily hotspots are then computed as the degrees above the MMM. DHW are finally computed as the cumulative hotspots exceeding 1°C in the past 12 weeks. If DHW exceed 4 °C weeks, the corals undergo a potential bleaching stress, and above 8 °C weeks they risk mortality. Our ability to predict bleaching and mortality is therefore conditioned by our capacity to accurately measure the DHW, and therefore, the MMM. Using various sources, products and time periods, we compared 14 different MMM values (Table II.2, Figure III.6.a). The MMM varied from 28.48°C (Fox et al. 2019; computed from the NOAA's Pathfinder v.5.2 product) computed from the NOAA's Pathfinder v.5.2 product) to 29.07 °C reached by the 2000-2020 climatology of the Copernicus ERA-5 reanalysis product. Apart from two sources (Fox et al. and Coral Reef Watch 50 m product before 2016), all MMM lie in the 29 ± 0.1°C range. To understand how MMM affect DHW, we computed the 2008-2017 maximum DHW reached by our in-situ data on the Forereef at Palmyra for various MMM values, ranging from 28.3 to 29.3, every 0.01 °C (Figure III.6.b). As expected, MMM widely affects the outcome of the heat stress computed. If the MMM is above 29°C, the DHW computed are close to zero, which would mean that the temperature never exceeded the threshold of MMM+1°C. Below an MMM of 29°C, the DHW vary linearly with MMM, the DHW are increasing as the MMM decreases, reaching the bleaching threshold for MMM below 28.81 °C and the mortality threshold for MMM below 28.63 °C. Among all the MMM we computed, only two out of fourteen values gave a DHW high enough to reach the bleaching threshold: the Coral Reef Watch 50km product, before 2016 and the one used in Fox et al. (2019); only the MMM from Fox et al. (2019) could have coincide with mortality at Palmyra. Given these perspectives, it would seem reasonable to consider the MMM to sit in the 29 ± 0.1°C range, which contradicts the bleaching observed at Palmyra during both the 2009 and the 2015 El Niño events (Williams et al. 2010; Furby et al. 2017; Fox

et al. 2019). This either shows that the method is incorrect for this study, or that there is an underlying process that is yet to be understood.

Table III.2 Maximum monthly means (MMM) computed from different sources and during different periods.

Source	Type	Specification	MMM*
Fox et al. 2019	Paper	From NOAA PFV5.2	28.48 °C
OiSSTv2	Satellite	1990-2010 (20 years)	28.96 °C
OiSSTv2	Satellite	2000-2020 (20 years)	29.06 °C
OiSSTv2	Satellite	1990-2020 (30 years)	29.03 °C
CRW	Satellite	50km before 2016	28.70 °C
CRW	Satellite	50km after 2016	29.00 °C
CRW	Satellite	5km	28.95 °C
ARGO	In-situ	2.5m deep 2005-2019	29.00 °C
ERA5	Reanalysis	1980-2000 (20 years)	28.96 °C
ERA5	Reanalysis	1990-2010 (20 years)	29.01 °C
ERA5	Reanalysis	2000-2020 (20 years)	29.07 °C
ERA5	Reanalysis	1980-2010 (30 years)	28.99 °C
ERA5	Reanalysis	1990-2020 (30 years)	29.05°C
ERA5	Reanalysis	1980-2020 (40 years)	29.01 °C

*Maximum monthly mean

Overall, it seems delicate to settle on which MMM is best to quantify heat stress at Palmyra atoll. Indeed, depending on the value used, the DHW could show various scenarios with all possible outcomes facing the 2015 event: 1) the heat stress was too high for such low mortality (Fox et al. 2019); 2) the heat stress was high enough to cause massive bleaching but low mortality, which would explain the observations solely based on temperature (CRW 50km before 2016); and 3) the heat stress was too low to cause such a widespread bleaching event, which raises a new problem (Using other CRW, ARGO, OiSST or ERA5). In the third scenario, excessive nutrients delivered by intensified upwelling could have exacerbated the coral susceptibility to bleaching (DeCarlo et al. 2020) which could explain why the reef bleached in 2015 with a limited heat stress. However, the limited heat stress reached in 2009 was not associated with intensified upwelling, and yet, bleaching and even some mortality was observed (Williams et al. 2010; Furby et al. 2017). It has been shown that the classical DHW definition is not always the most adapted to quantify heat stress on coral reefs (DeCarlo 2020), and sometimes other methods are preferred (e.g. percentile based MMM at Jarvis island, Barkley et al. (2018)). Our ability to accurately predict bleaching and mortality at this location remains low using the classical heat stress bleaching. A locally adapted definition based on the local colonies' history, combined with metrics from processes other than temperature only would benefit coral research in this atoll.
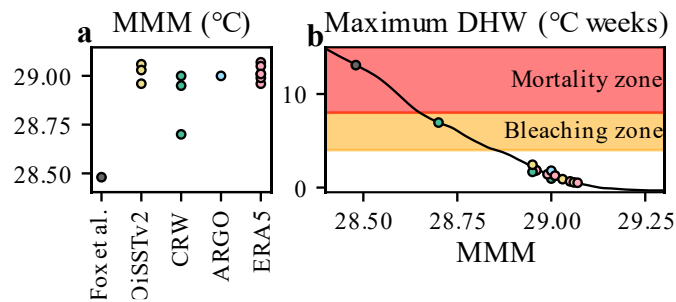
Figure III.6 (**a**) Maximum monthly mean (MMM) at Palmyra atoll computed from different sources and temporal periods (Table X). The colour of the circles represents the sources. (**b**) Maximum degree heating weeks (DHW) reached in the shallow water of the forereef at Palmyra atoll during the 2015 El Niño event compared to the MMM used as a threshold. DHW were computed over all locations and depths on the forereef at Palmyra, and then the 2008-2017 maxima were extracted for each MMM. The circles represent how much DHW were computed by the methods in (a), and their colour represents the method.

III.4.2   ENSO-induced strong upwelling events

We showed that an extreme upwelling event happened at Palmyra during the 2015 El Niño. These events seem to be a feature of very strong el Niño events and their transition state to La Niña.

High-frequency upwelling in the area is mostly caused by shoaling internal waves, breaking on islands and atolls bathymetry (Kao et al. 1985; Sutherland et al. 2013; Woodson 2018). At all locations studied, shallower thermoclines were associated with increasingly intensified upwelling. The highest recorded DCW values were always linked with thermoclines shallower than 60m, and the corresponded to the shallowest thermoclines at Palmyra, Kingman and Jarvis. We also showed that at all locations except Baker, upwelling intensity displayed a lower limit when thermocline was shallower than 80 m. This limit increases with shallower thermoclines, reaching almost 1°C weeks when the thermocline was shallower than 50 m. A shallower thermocline reduces the distance shoaling internal waves need to travel before reaching nearshore ecosystems and therefore the energy they require to propagate, thus increasing both the intensity and the frequency of the events.

Combining our previous findings, we suggest that very strong El Niño and their following La Niña phases can produce extreme upwelling events in the tropical Pacific, which can ultimately affect nearshore ecosystems. The thermocline shoaling patterns previously exposed induced intensified upwelling North of the equator in November during the very strong El Niño and on the Equator during the following La Niña. Our ten-year record of upwelling intensity at the five locations studied show that 1) during the 2015 El Niño, considered very strong, Palmyra and Kingman saw island-wide extreme upwelling event matching their shallowest thermocline of the decade, and 2) during the La Niña phase following the 2015 and the 2009 El Niño, which was a strong event, Howland, Jarvis and Baker saw extreme upwelling periods, also matching the two shallowest thermoclines of the decade. Very strong El

Niño and their following La Niña can generate upwelling-exposed areas in the tropical Pacific, ultimately affecting nearshore ecosystems (Woodson 2018). If the heat stress undergone by the corals at Palmyra is acknowledged, the reef could have been saved by this El Niño-induced upwelling event. Inversely, El Niño can also prevent upwelling in certain areas. During the 2015 El Niño, upwelling at Jarvis island was stopped (Figure III.3.c), despite Jarvis being constantly exposed to upwelling through the Equatorial Undercurrent (Gove et al. 2006). This was associated with a thermocline deeper than the climatology (Figure III.3.k, Figure III.5.c;d;g). The interruption of nutrient supply associated with a massive heat stress led to one of the worst mortality rates on records for the coral reefs at Jarvis (Vargas-Ángel et al. 2019). Similarly, Darwin and Wolf islands, in the Northern Galapagos (92°W, 1.5°N), are usually subject to upwelling, bringing nutrients and cool water to their coral reefs. During the 1997/1998 El Niño, the coral community bleached while very little bleaching was recorded after the 2015 El Niño. The difference was associated with an interruption of upwelling during the 1997 events while upwelling remained active during the 2015 event (Riegl et al. 2019). These findings match the thermocline depth data from the NCEP-GODAS product (Figure III.7). During the 1997/1998 El Niño, the thermocline deepened to 55m, 22m below the climatologically deepest month (33m). During the 2015/2016 El Niño, the thermocline also deepened but only down to 40m.
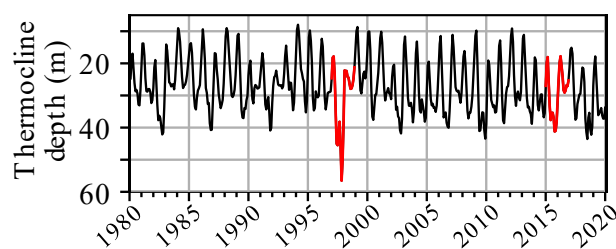
Figure III.7 Three month rolling NCEP-GODAS thermocline depth at Darwin and Wolf islands in the Northern Galapagos (92°W, 1.5°N). Thermocline depths during the 1997/1998 and 2015/2016 El Niño events are highlighted by the red solid lines.

Our findings are based on averages of each ENSO phase years. However, observed thermocline variability, linked with potential upwelling intensification or deprivation can be inconsistent from one event to another in certain locations, as it is the case for the Galapagos islands. This provides an uncertainty which toughens the predictability of such events. Through important changes in the thermocline depth, very strong El Niño and their following a Niña can redistribute upwelling-exposed areas during heat waves in the tropical Pacific. These changes can profoundly impact nearshore ecosystems in both a positive and a negative way. Extreme sudden upwelling events can give a temporary shelter to previously exposed ecosystems facing heat stress, like in Palmyra during the 2015 El Niño, through thermal relief (Schmidt et al. 2016; Wyatt et al. 2020) and nutrient delivery (Riegl et al. 2019). However, in some cases like in the

Red Sea, excessive nutrient supply can also worsen the effects of heat stress on reefs, increasing their vulnerability and facilitating bleaching (Wiedenmann et al. 2013; DeCarlo et al. 2020; Burkepile et al. 2020). Nutrient-enriched area, immersed in almost constant upwelling can also see a deepening of the thermocline leading to the interruption of upwelling, like at Jarvis or in the Galapagos. This process cuts an important source of food for the corals which can have devastating effects. With an already going increase in both the frequency and intensity of El Niño events, lucky - or unlucky - reefs could theoretically see the future trajectory of their corals be disturbed by such upwelling events in the near future. A better understanding of this temporary redistribution of upwelling-exposed areas could provide an insight on unsuspected naturally sheltered coral reef, which should be focused on by conservation strategies.

Chapter IV.   Conclusion

Upwelling is a physical process able to influence greatly the response of coral reefs to heat stress. Through this piece of work, we first presented a new algorithm that allows systematic study of upwelling dynamics in various geographical contexts and periods of studies. This new method, based on a temperature stratification index improves the detection rate of upwelling-induced cold pulses, but also the human processing time as it is fully automatic. This algorithm could be adapted to the detection and quantification of various advection processes, whether they are linked with downwelling, upwelling or sideways transport, as long as there are measurable differences between two water masses.

Using this newly developed method, we identified interconnections between ENSO, thermocline depth and upwelling intensity. We showed that very strong El Niño events and their following La Niña widely affect thermocline depth on a basin-wide scale. The thermocline shoaling patterns were associated with intensified upwelling areas in the tropical Pacific. Overall, we show that, through their effects on thermocline depth, very strong El Niño events and their following La Niña redistribute upwelling-exposed areas, creating and eliminating temporary thermal refugees for nearshore environments. In our changing climate a better understanding of this ENSO-induced upwelling variability could provide insight on naturally sheltered areas, that should be the focus of some conservation efforts in the future.

References

Alford, M. H., T. Peacock, J. A. Mackinnon, and others. 2015. The formation and fate of internal waves in the South China Sea. Nature **521**: 65–69. doi:10.1038/nature14399

Altieri, A. H., S. B. Harrison, J. Seemann, R. Collin, R. J. Diaz, and N. Knowlton. 2017. Tropical dead zones and mass mortalities on coral reefs. Proc. Natl. Acad. Sci. U. S. A. **114**: 3660–3665. doi:10.1073/pnas.1621517114

Anneken, M., Y. Fischer, and J. Beyerer. 2015. Evaluation and comparison of anomaly detection algorithms in annotated datasets from the maritime domain. *IntelliSys 2015 - Proceedings of 2015 SAI Intelligent Systems Conference.* Institute of Electrical and Electronics Engineers Inc. 169–178.

Aston, E. A., G. J. Williams, J. A. M. Green, and others. 2019. Scale-dependent spatial patterns in benthic communities around a tropical island seascape. Ecography (Cop.). **42**: 578–590. doi:10.1111/ecog.04097

Barkley, H. C., A. L. Cohen, N. R. Mollica, and others. 2018. Repeat bleaching of a central Pacific coral reef over the past six decades (1960–2016). Commun. Biol. **1**. doi:10.1038/s42003-018-0183-7

Behringer, D., and Y. Xue. 2004. Evaluation of the global ocean data assimilation system at NCEP: The Pacific Ocean. *Proc. Eighth Symp. on Integrated Observing and Assimilation Systems for Atmosphere, Oceans, and Land Surface.* 11–15.

Buerger, P., G. M. Schmidt, M. Wall, C. Held, and C. Richter. 2015. Temperature tolerance of the coral Porites lutea exposed to simulated large amplitude internal waves (LAIW). J. Exp. Mar. Bio. Ecol. **471**: 232–239. doi:10.1016/j.jembe.2015.06.014

Burkepile, D. E., A. A. Shantz, T. C. Adam, and others. 2020. Nitrogen Identity Drives Differential Impacts of Nutrients on Coral Bleaching and Mortality. Ecosystems **23**: 798–811. doi:10.1007/s10021-019-00433-2

Comfort, C. M., G. O. Walker, M. A. McManus, A. G. Fujimura, C. E. Ostrander, and T. J. Donaldson. 2019. Physical dynamics of the reef flat, channel, and fore reef areas of a fringing reef embayment: An oceanographic study of Pago Bay, Guam. Reg. Stud. Mar. Sci. **31**. doi:10.1016/j.rsma.2019.100740

DeCarlo, T. M. 2020. Treating coral bleaching as weather: a framework to validate and optimize prediction skill. PeerJ **8**: e9449. doi:10.7717/peerj.9449

DeCarlo, T. M., L. Gajdzik, J. Ellis, and others. 2020. Nutrient-supplying ocean currents modulate coral bleaching susceptibility. Sci. Adv **6**.

Donner, S. D., G. J. M. Rickbeil, and S. F. Heron. 2017. A new, high-resolution global mass coral bleaching database. PLoS One **12**. doi:10.1371/journal.pone.0175490

Espinoza-Morriberón, D., V. Echevin, F. Colas, J. Tam, J. Ledesma, L. Vásquez, and M. Graco. 2017. Impacts of El Niño events on the Peruvian upwelling system productivity. J. Geophys. Res. Ocean. **122**: 5423–5444. doi:10.1002/2016JC012439

Fox, M. D., A. L. Carter, C. B. Edwards, and others. 2019. Limited coral mortality following acute thermal stress and widespread bleaching on Palmyra Atoll, central Pacific. Coral Reefs **38**: 701–712. doi:10.1007/s00338-019-01796-7

Fox, M. D., G. J. Williams, M. D. Johnson, and others. 2018. Gradients in Primary Production Predict Trophic Strategies of Mixotrophic Corals across Spatial Scales. Curr. Biol. **28**: 3355-3363.e4.

doi:10.1016/j.cub.2018.08.057

Fujita, R. M. 1985. The role of nitrogen status in regulating transient ammonium uptake and nitrogen storage by macroalgae. J. Exp. Mar. Bio. Ecol. **92**: 283–301.

Furby, K. A., J. E. Smith, and S. A. Sandin. 2017. Porites superfusa mortality and recovery from a bleaching event at Palmyra Atoll, USA. PeerJ **2017**. doi:10.7717/peerj.3204

Glynn, P. W. 1984. Widespread Coral Mortality and the 1982–83 El Niño Warming Event. Environ. Conserv. **11**: 133–146. doi:10.1017/S0376892900013825

Gove, J. M., M. A. McManus, A. B. Neuheimer, and others. 2016. Near-island biological hotspots in barren ocean basins. Nat. Commun. **7**. doi:10.1038/ncomms10581

Gove, J. M., M. A. Merrifield, and R. E. Brainard. 2006. Temporal variability of current-driven upwelling at Jarvis Island. J. Geophys. Res. Ocean. **111**. doi:10.1029/2005JC003161

Gove, J. M., G. J. Williams, M. A. Mcmanus, S. J. Clark, J. S. Ehses, and L. M. Wedding. 2015. Coral reef benthic regimes exhibit non-linear threshold responses to natural physical drivers. Source Mar. Ecol. Prog. Ser. **522**: 33–48. doi:10.2307/24895091

Den Haan, J., J. Huisman, H. J. Brocke, and others. 2016. Nitrogen and phosphorus uptake rates of different species from a coral reef community after a nutrient pulse. Sci. Rep. **6**. doi:10.1038/srep28821

Hoegh-Guldberg, O. 1999. Climate change, coral bleaching and the future of the world's coral reefs. Mar. Freshw. Res. **50**: 839–866. doi:10.1071/MF99078

Hoegh-Guldberg, O., P. J. Mumby, A. J. Hooten, and others. 2007. Coral Reefs Under Rapid Climate Change and Ocean Acidification. Science (80-.). **318**: 1737–1742.

Hughes, T. P., J. T. Kerry, M. Álvarez-Noriega, and others. 2017. Global warming and recurrent mass bleaching of corals. Nature **543**: 373–377. doi:10.1038/nature21707

Hughes, T. P., J. T. Kerry, A. H. Baird, and others. 2018. Global warming transforms coral reef assemblages. Nature **556**: 492–496. doi:10.1038/s41586-018-0041-2

Ji, C., X. Zou, S. Liu, and L. Pan. 2019. ADARC: An anomaly detection algorithm based on relative outlier distance and biseries correlation. Softw. - Pract. Exp. doi:10.1002/spe.2756

Kao, T. W., F. S. Pan, and D. Renouard. 1985. Internal solitons on the pycnocline: Generation, propagation, and shoaling and breaking over a slope. J. Fluid Mech. **159**: 19–53. doi:10.1017/S0022112085003081

Kuo, N. J., Q. Zheng, and C. R. Ho. 2004. Response of Vietnam coastal upwelling to the 1997-1998 ENSO event observed by multisensor data. Remote Sens. Environ. **89**: 106–115. doi:10.1016/j.rse.2003.10.009

Ladah, L. B., A. Filonov, M. F. Lavín, J. J. Leichter, J. A. Zertuche-González, and D. M. Pérez-Mayorga. 2012. Cross-shelf transport of sub-thermocline nitrate by the internal tide and rapid (3-6h) incorporation by an inshore macroalga. Cont. Shelf Res. **42**: 10–19. doi:10.1016/j.csr.2012.03.010

Leichter, J. J., and S. J. Genovese. 2006. Intermittent upwelling and subsidized growth of the scleractinian coral Madracis mirabilis on the deep fore-reef slope of Discovery Bay, Jamaica. Mar. Ecol. Prog. Ser. **316**: 95–103.

Leichter, J. J., H. L. Stewart, S. L. Miller, and others. 2003. Episodic nutrient transport to Florida coral reefs. Limnol. Oceanogr. **48**: 1394–1407.

Leichter, J. J., S. R. Wing, S. L. Miller, and M. W. Denny. 1996. Pulsed delivery of subthermocline water to Conch Reef (Florida Keys) by internal tidal bores.

Li, Y., X. Zhong, Z. Ma, and H. Liu. 2020. The outlier and integrity detection of rail profile based on profile registration. IEEE Trans. Intell. Transp. Syst. **21**: 1074–1085. doi:10.1109/TITS.2019.2901633

Manzello, D. P. 2010. Coral growth with thermal stress and ocean acidification: Lessons from the eastern tropical Pacific. Coral Reefs **29**: 749–758. doi:10.1007/s00338-010-0623-4

McPhaden, M. J. 2015. Playing hide and seek with El Niño. Nat. Clim. Chang. **5**: 791–795. doi:10.1038/nclimate2775

McPhaden, M. J., T. Lee, and D. McClurg. 2011. El Niño and its relationship to changing background conditions in the tropical Pacific Ocean. Geophys. Res. Lett. **38**. doi:10.1029/2011GL048275

Miller, J., J. Maragos, R. Brainard, and others. 2008. The state of coral reef ecosystems of the Pacific Remote Island Areas. state coral reef Ecosyst. United States Pacific Free. Assoc. States.

Monismith, S. G., A. Genin, M. A. Reidenbach, G. Yahel, and J. R. Koseff. 2006. Thermally driven exchanges between a coral reef and the adjoining ocean. J. Phys. Oceanogr. **36**: 1332–1347. doi:10.1175/JPO2916.1

Montecinos, A., and F. Gomez. 2010. ENSO modulation of the upwelling season off southern-central Chile. Geophys. Res. Lett. **37**. doi:10.1029/2009GL041739

Pacherres, C. O., G. M. Schmidt, and C. Richter. 2013. Autotrophic and heterotrophic responses of the coral Porites lutea to large amplitude internal waves. J. Exp. Biol. **216**: 4365–4374. doi:10.1242/jeb.085548

Pineda, J. 1991. Predictable upwelling and the shoreward transport of planktonic larvae by internal tidal bores. Science (80-.). **253**: 548–549.

Radice, V. Z., O. Hoegh-Guldberg, B. Fry, M. D. Fox, and S. G. Dove. 2019. Upwelling as the major source of nitrogen for shallow and deep reef-building corals across an oceanic atoll system. Funct. Ecol. **33**: 1120–1134. doi:10.1111/1365-2435.13314

Randall, C. J., L. T. Toth, J. J. Leichter, J. L. Maté, and R. B. Aronson. 2020. Upwelling buffers climate change impacts on coral reefs of the eastern tropical Pacific. Ecology **101**. doi:10.1002/ecy.2918

Rao, R. R., and R. Sivakumar. 2000. Seasonal variability of near-surface thermal structure and heat budget of the mixed layer of the tropical Indian Ocean from a new global ocean temperature climatology. J. Geophys. Res. Ocean. **105**: 995–1015. doi:10.1029/1999jc900220

Raven, J. A., and R. Taylor. 2003. Macroalgal growth in nutrient-enriched estuaries: a biogeochemical and evolutionary perspective. Water, Air Soil Pollut. Focus **3**: 7–26.

Reid, E. C., T. M. DeCarlo, A. L. Cohen, G. T. F. Wong, S. J. Lentz, A. Safaie, A. Hall, and K. A. Davis. 2019. Internal waves influence the thermal and nutrient environment on a shallow coral reef. Limnol. Oceanogr. **64**: 1949–1965. doi:10.1002/lno.11162

Riegl, B., P. W. Glynn, S. Banks, I. Keith, F. Rivera, M. Vera-Zambrano, C. D'Angelo, and J. Wiedenmann. 2019. Heat attenuation and nutrient delivery by localized upwelling avoided coral bleaching mortality in northern Galapagos during 2015/2016 ENSO. Coral Reefs **38**: 773–785.

doi:10.1007/s00338-019-01787-8

Roder, C., L. Fillinger, C. Jantzen, G. M. Schmidt, S. Khokiattiwong, and C. Richter. 2010. Trophic response of Corals to large amplitude internal waves. Mar. Ecol. Prog. Ser. **412**: 113–128. doi:10.3354/meps08707

Ross, O. N., and J. Sharples. 2007. Phytoplankton motility and the competition for nutrients in the thermocline. Mar. Ecol. Prog. Ser. **347**: 21–38. doi:10.3354/meps06999

Safaie, A., N. J. Silbiger, T. R. McClanahan, and others. 2018. High frequency temperature variability reduces the risk of coral bleaching. Nat. Commun. **9**. doi:10.1038/s41467-018-04074-2

Sakai, K., T. Singh, and A. Iguchi. 2019. Bleaching and post-bleaching mortality of Acropora corals on a heat-susceptible reef in 2016. PeerJ **2019**. doi:10.7717/peerj.8138

Schmidt, G. M., M. Wall, M. Taylor, C. Jantzen, and C. Richter. 2016. Large-amplitude internal waves sustain coral health during thermal stress. Coral Reefs **35**: 869–881. doi:10.1007/s00338-016-1450-z

Sevadjian, J. C., M. A. McManus, K. J. Benoit-Bird, and K. E. Selph. 2012. Shoreward advection of phytoplankton and vertical re-distribution of zooplankton by episodic near-bottom water pulses on an insular shelf: Oahu, Hawaii. Cont. Shelf Res. **50–51**: 1–15. doi:10.1016/j.csr.2012.09.006

Simpson, J. H., and R. D. Pingree. 1978. Shallow sea fronts produced by tidal stirring, p. 29–42. *In* Oceanic fronts in coastal processes.

Storlazzi, C. D., O. M. Cheriton, R. van Hooidonk, Z. Zhao, and R. Brainard. 2020. Internal tides can provide thermal refugia that will buffer some coral reefs from future global warming. Sci. Rep. **10**: 13435. doi:10.1038/s41598-020-70372-9

Sutherland, B. R., K. J. Barrett, and G. N. Ivey. 2013. Shoaling internal solitary waves. J. Geophys. Res. Ocean. **118**: 4111–4124. doi:10.1002/jgrc.20291

Trenberth, K. E. 1997. The definition of El Nino. Bull. Am. Meteorol. Soc. **78**: 2771–2778.

Vargas-Ángel, B., B. Huntington, R. E. Brainard, R. Venegas, T. Oliver, H. Barkley, and A. Cohen. 2019. El Niño-associated catastrophic coral mortality at Jarvis Island, central Equatorial Pacific. Coral Reefs **38**: 731–741. doi:10.1007/s00338-019-01838-0

Vargas-Ángel, B., E. E. Looney, O. J. Vetter, and E. F. Coccagna. 2011. Severe, widespread El Niño-associated coral bleaching in the US Phoenix Islands. Bull. Mar. Sci. **87**: 623–638. doi:10.5343/bms.2010.1095

Wall, M., G. M. Schmidt, P. Janjang, S. Khokiattiwong, and C. Richter. 2012. Differential Impact of Monsoon and Large Amplitude Internal Waves on Coral Reef Development in the Andaman Sea. PLoS One **7**. doi:10.1371/journal.pone.0050207

Walter, R. K., C. Brock Woodson, R. S. Arthur, O. B. Fringer, and S. G. Monismith. 2012. Nearshore internal bores and turbulent mixing in southern Monterey Bay. J. Geophys. Res. Ocean. **117**. doi:10.1029/2012JC008115

Walter, R. K., C. B. Woodson, P. R. Leary, and S. G. Monismith. 2014. Connecting wind-driven upwelling and offshore stratification to nearshore internal bores and oxygen variability. J. Geophys. Res. Ocean. **119**: 3517–3534. doi:10.1002/2014JC009998

Wiedenmann, J., C. D'Angelo, E. G. Smith, A. N. Hunt, F. E. Legiret, A. D. Postle, and E. P. Achterberg. 2013. Nutrient enrichment can increase the susceptibility of reef corals to bleaching.

Nat. Clim. Chang. **3**: 160–164. doi:10.1038/nclimate1661

Williams, G. J., I. S. Knapp, J. E. Maragos, and S. K. Davy. 2010. Modeling patterns of coral bleaching at a remote Central Pacific atoll. Mar. Pollut. Bull. **60**: 1467–1476. doi:10.1016/j.marpolbul.2010.05.009

Williams, G. J., S. A. Sandin, B. J. Zgliczynski, and others. 2018. Biophysical drivers of coral trophic depth zonation. Mar. Biol. **165**. doi:10.1007/s00227-018-3314-2

Woodson, C. B. 2018. The Fate and Impact of Internal Waves in Nearshore Ecosystems. Ann. Rev. Mar. Sci. **10**: 421–441. doi:10.1146/annurev-marine-121916

Wyatt, A. S. J., J. J. Leichter, L. T. Toth, T. Miyajima, R. B. Aronson, and T. Nagata. 2020. Heat accumulation on coral reefs mitigated by internal waves. Nat. Geosci. **13**: 28–34. doi:10.1038/s41561-019-0486-4

Xu, K., R. X. Huang, W. Wang, C. Zhu, and R. Lu. 2017. Thermocline fluctuations in the equatorial pacific related to the two types of El Niño events. J. Clim. **30**: 6611–6627. doi:10.1175/JCLI-D-16-0291.1

Yang, G., L. Liu, X. Zhao, Y. Li, Y. Duan, B. Liu, K. Huang, and W. Yu. 2019. Impacts of Different Types of ENSO Events on Thermocline Variability in the Southern Tropical Indian Ocean. Geophys. Res. Lett. **46**: 6775–6785. doi:10.1029/2019GL082818

Yeh, S. W., J. S. Kug, B. Dewitte, M. H. Kwon, B. P. Kirtman, and F. F. Jin. 2009. El Niño in a changing climate. Nature **461**: 511–514. doi:10.1038/nature08316

Zhang, X., and M. J. McPhaden. 2006. Wind stress variations and interannual sea surface temperature anomalies in the eastern equatorial Pacific. J. Clim. **19**: 226–241. doi:10.1175/JCLI3618.1

Supplementary material

Table S1 Details of temperature loggers used in the study.

[1] SeaBird Electronics© SBE56 or SBE39 [2] SeaBird Electronics© SBE37 [3] Sea surface temperature buoys

Site ID	Island	Latitude (°N)	Longitude(°E)	Depth (m)	Logger type	Start	End	Sampling frequency (s)
OCC-BAK-001	Baker	0,206355	-176,475981	25,2	STR[1]	17-03-2012 03:00:00	31-05-2012 09:00:00	3600
OCC-BAK-001	Baker	0,20636	-176,475921	25,6	STR	09-02-2015 19:39:59	14-06-2018 10:19:59	300
OCC-BAK-002	Baker	0,204922	-176,476496	14,1	STR	17-03-2012 03:00:00	08-02-2015 21:00:00	3600
OCC-BAK-002	Baker	0,204946	-176,476516	13,7	STR	09-02-2015 01:34:59	19-09-2016 13:29:59	300
OCC-BAK-004	Baker	0,191586	-176,456458	24,9	STR	16-03-2012 05:00:00	10-02-2015 21:00:00	3600
OCC-BAK-004	Baker	0,191548	-176,456438	24,7	STR	10-02-2015 21:04:59	12-04-2016 14:09:59	300
OCC-BAK-005	Baker	0,191565	-176,460137	15,2	STR	16-03-2012 04:00:00	10-02-2015 00:00:00	3600
OCC-BAK-005	Baker	0,191589	-176,460124	14,4	STR	10-02-2015 00:14:59	23-06-2016 05:04:59	300
OCC-BAK-006	Baker	0,194095	-176,467264	5,3	STR	15-03-2012 23:00:00	10-02-2015 01:00:00	3600
OCC-BAK-006	Baker	0,194085	-176,467248	4,7	STR	10-02-2015 01:09:59	13-06-2018 02:39:59	300
OCC-BAK-009	Baker	0,191728	-176,488894	25,3	STR	17-03-2012 22:00:00	08-02-2015 17:00:00	3600
OCC-BAK-009	Baker	0,191715	-176,488912	27,7	STR	08-02-2015 20:24:59	05-11-2016 07:09:59	300
OCC-BAK-010	Baker	0,191712	-176,488808	16,8	STR	24-01-2004 20:30:00	27-06-2005 00:30:58	1800
OCC-BAK-010	Baker	0,191813	-176,488696	14,1	STR	11-04-2017 03:04:59	12-06-2018 21:19:59	300
OCC-BAK-010	Baker	0,191792	-176,488728	14,7	STR	10-02-2015 12:49:59	30-12-2016 20:14:59	300
OCC-BAK-012	Baker	0,191652	-176,488471	4,47	STR	31-01-2006 03:00:00	09-02-2008 01:00:02	1800
OCC-BAK-012	Baker	0,191635	-176,488497	4,6	STR	24-01-2004 20:30:00	01-12-2005 20:59:59	1800
OCC-BAK-012	Baker	0,1917	-176,488511	4,58	STR	09-02-2008 02:00:00	07-02-2010 01:30:00	1800
OCC-BAK-014	Baker	0,194573	-176,462828	11,4	STR	11-02-2010 15:30:00	17-11-2011 20:00:01	1800
OCC-BAK-015	Baker	0,205378	-176,47574	18,29	STR	24-01-2004 23:29:59	05-06-2005 19:29:59	1800
OCC-BAK-015	Baker	0,205386	-176,475932	17,5	STR	07-02-2010 22:00:00	16-03-2012 22:00:00	1800
OCC-BAK-015	Baker	0,205395	-176,475786	16,96	STR	02-02-2006 00:00:00	10-02-2008 01:00:00	1800
OCC-BAK-015	Baker	0,205414	-176,475874	16,97	STR	10-02-2008 03:00:00	07-02-2010 21:00:00	1800
OCC-BAK-016	Baker	0,187837	-176,474756	5,4	STR	07-02-2010 03:00:00	16-03-2012 03:00:01	1800
OCC-BAK-016	Baker	0,18789	-176,474745	4,52	STR	31-01-2006 01:30:00	09-02-2008 22:00:00	1800
OCC-BAK-016	Baker	0,187871	-176,474749	4,88	STR	10-02-2008 07:00:00	07-02-2010 02:30:00	1800
OCC-BAK-017	Baker	0,19179	-176,488645	9,1	STR	07-02-2010 02:00:00	17-03-2012 02:30:00	1800
OCC-BAK-018	Baker	0,191731	-176,488769	17,57	STR	31-01-2006 02:30:00	09-02-2008 01:00:00	1800
OCC-BAK-018	Baker	0,191773	-176,488743	17,78	STR	09-02-2008 03:00:00	07-02-2010 00:30:00	1800
OCC-BAK-018	Baker	0,191788	-176,488679	18,6	STR	07-02-2010 01:00:00	17-03-2012 03:00:00	1800
OCC-BAK-019	Baker	0,19005	-176,46025	18,9	SBE37[2]	01-02-2002 09:00:00	15-12-2003 21:44:59	900
OCC-BAK-019	Baker	0,19005	-176,46025	18,9	SBE37	23-01-2004 22:30:01	23-01-2005 05:30:01	1800
OCC-BAK-019	Baker	0,189907	-176,460129	19,91	SBE37	09-02-2008 22:00:00	06-02-2010 20:00:01	1800
OCC-BAK-021	Baker	0,187967	-176,47474	2,4	STR	24-01-2004 02:00:00	28-07-2004 13:30:00	1800
OCC-HOW-002	Howland	0,809322	-176,61042	24,9	STR	12-03-2012 06:00:00	17-02-2014 16:00:00	3600
OCC-HOW-002	Howland	0,809365	-176,610451	25	STR	04-02-2015 21:04:59	06-04-2016 03:54:59	300
OCC-HOW-003	Howland	0,809322	-176,610596	14,8	STR	12-03-2012 08:00:00	07-09-2013 09:00:00	3600
OCC-HOW-003	Howland	0,809348	-176,610588	14,4	STR	11-04-2017 22:04:59	09-06-2018 22:19:59	300

Site ID	Island	Latitude (°N)	Longitude(°E)	Depth (m)	Logger type	Start	End	Sampling frequency (s)
OCC-HOW-003	Howland	0,809345	-176,610602	14,5	STR	04-02-2015 21:14:59	23-10-2016 01:24:59	300
OCC-HOW-004	Howland	0,809188	-176,610835	5,2	STR	13-03-2012 21:00:00	04-02-2015 23:00:00	3600
OCC-HOW-004	Howland	0,809128	-176,610977	5,2	STR	05-02-2015 02:14:59	21-12-2017 07:29:59	300
OCC-HOW-006	Howland	0,806505	-176,621533	25	STR	05-02-2015 19:24:59	11-05-2017 14:04:52	300
OCC-HOW-007	Howland	0,806539	-176,621481	15,3	STR	15-03-2012 01:00:00	05-02-2015 15:00:00	3600
OCC-HOW-007	Howland	0,806549	-176,621481	14,3	STR	12-04-2017 02:24:59	09-06-2018 01:44:59	300
OCC-HOW-007	Howland	0,806554	-176,621482	14,7	STR	05-02-2015 19:29:59	01-03-2017 00:54:59	300
OCC-HOW-008	Howland	0,806603	-176,621336	3,02	STR	28-01-2006 22:00:00	07-02-2008 00:00:02	1800
OCC-HOW-008	Howland	0,806591	-176,621356	3	STR	21-01-2004 23:00:00	24-01-2006 20:00:01	1800
OCC-HOW-008	Howland	0,80659	-176,621383	4,9	STR	12-03-2012 22:00:00	27-12-2014 01:00:00	3600
OCC-HOW-008	Howland	0,806605	-176,621354	4,2	STR	03-02-2010 21:00:00	12-03-2012 21:30:00	1800
OCC-HOW-008	Howland	0,806608	-176,621343	3,47	STR	07-02-2008 12:00:00	03-02-2010 20:30:00	1800
OCC-HOW-008	Howland	0,806587	-176,621404	5,2	STR	05-02-2015 22:54:59	17-01-2017 14:54:59	300
OCC-HOW-009	Howland	0,814806	-176,623984	14,82	STR	07-02-2008 23:30:00	03-02-2010 21:00:00	1800
OCC-HOW-009	Howland	0,814818	-176,623928	15,2	STR	03-02-2010 21:30:00	11-03-2012 20:00:00	1800
OCC-HOW-010	Howland	0,806467	-176,621633	38	STR	28-10-2006 22:00:00	07-02-2008 23:30:00	1800
OCC-HOW-010	Howland	0,806476	-176,621583	37,59	STR	08-02-2008 03:00:00	03-02-2010 19:30:00	1800
OCC-HOW-011	Howland	0,806476	-176,621645	18,59	STR	28-01-2006 22:00:00	05-02-2008 23:30:01	1800
OCC-HOW-011	Howland	0,806481	-176,621584	18,7	STR	21-01-2004 23:00:00	25-01-2006 08:00:00	1800
OCC-HOW-011	Howland	0,806468	-176,621522	19,8	STR	03-02-2010 20:00:00	12-03-2012 20:00:00	1800
OCC-HOW-011	Howland	0,806505	-176,621509	18,59	STR	07-02-2008 12:00:00	03-02-2010 19:30:00	1800
OCC-HOW-012	Howland	0,82351	-176,62216	18,9	STR	22-01-2004 23:00:00	26-02-2006 15:30:00	1800
OCC-JAR-002	Jarvis	-0,367639	-159,978816	24,5	STR	10-04-2015 11:54:59	30-07-2018 01:34:59	300
OCC-JAR-003	Jarvis	-0,367768	-159,978811	15,1	STR	13-11-2015 12:50:05	18-05-2016 09:05:05	300
OCC-JAR-003	Jarvis	-0,367753	-159,978816	15,5	STR	18-05-2016 21:39:27	02-04-2017 22:24:27	300
OCC-JAR-003	Jarvis	-0,367764	-159,978808	14,9	STR	10-04-2015 00:39:59	12-11-2015 22:59:59	300
OCC-JAR-003	Jarvis	-0,367668	-159,97882	14,7	STR	04-04-2017 02:24:59	30-07-2018 11:09:59	300
OCC-JAR-004	Jarvis	-0,375102	-159,972299	24,5	STR	09-04-2015 00:49:59	28-07-2018 23:44:59	300
OCC-JAR-004	Jarvis	-0,375062	-159,972331	24,9	STR	05-05-2012 01:01:59	08-04-2015 20:16:59	60
OCC-JAR-005	Jarvis	-0,375112	-159,972473	13,2	STR	09-04-2015 07:09:59	29-07-2018 19:29:59	300
OCC-JAR-005	Jarvis	-0,375096	-159,972482	14,2	STR	05-05-2012 00:59:59	08-04-2015 21:18:59	60
OCC-JAR-006	Jarvis	-0,373945	-159,983394	5,1	STR	19-05-2016 00:58:14	29-07-2018 12:18:14	300
OCC-JAR-006	Jarvis	-0,373939	-159,983417	4,8	STR	13-11-2015 17:51:52	18-05-2016 12:56:52	300
OCC-JAR-006	Jarvis	-0,373936	-159,983422	4,9	STR	09-04-2015 02:39:59	12-11-2015 22:59:59	300
OCC-JAR-006	Jarvis	-0,373966	-159,983391	5,1	STR	05-05-2012 03:22:59	08-04-2015 21:47:59	60
OCC-JAR-007	Jarvis	-0,382443	-160,002952	24,5	STR	10-04-2015 02:09:59	31-07-2018 17:39:59	300
OCC-JAR-008	Jarvis	-0,382343	-160,003032	14	STR	10-04-2015 05:19:59	04-04-2017 20:09:59	300
OCC-JAR-008	Jarvis	-0,382347	-160,002983	14,6	STR	05-04-2017 02:24:59	31-07-2018 00:49:59	300
OCC-JAR-009	Jarvis	-0,381563	-160,002884	5,2	STR	09-04-2015 21:39:59	26-11-2017 19:09:59	300
OCC-JAR-010	Jarvis	-0,379132	-160,015433	15,04	SBE37	20-03-2006 19:59:59	26-03-2008 20:00:00	1800
OCC-JAR-010	Jarvis	-0,37916	-160,015511	14,87	SBE37	10-03-2002 03:00:01	09-12-2003 15:15:01	900
OCC-JAR-010	Jarvis	-0,379136	-160,015462	14,8	SBE37	26-03-2004 22:30:12	23-01-2006 13:30:11	1800
OCC-JAR-010	Jarvis	-0,379188	-160,015438	14,62	SBE37	26-03-2008 21:30:00	01-04-2010 21:00:01	1800
OCC-JAR-010	Jarvis	-0,379253	-160,015518	15,23	STR	27-03-2008 12:00:00	01-04-2010 21:00:00	1800
OCC-JAR-010	Jarvis	-0,379239	-160,015506	15,2	STR	01-04-2010 21:30:00	04-05-2012 00:00:00	1800

Site ID	Island	Latitude (°N)	Longitude(°E)	Depth (m)	Logger type	Start	End	Sampling frequency (s)
OCC-JAR-010	Jarvis	-0,379222	-160,015448	15	STR	12-04-2015 02:24:59	27-11-2017 12:49:59	300
OCC-JAR-012	Jarvis	-0,368913	-160,008207	22,5	SBE37	01-04-2010 20:22:31	05-04-2010 20:15:01	90
OCC-JAR-012	Jarvis	-0,368923	-160,008249	24,9	STR	03-05-2012 21:35:59	10-04-2015 22:58:59	60
OCC-JAR-012	Jarvis	-0,368917	-160,008239	24,4	STR	12-11-2015 23:04:10	20-05-2016 10:54:10	300
OCC-JAR-012	Jarvis	-0,368945	-160,008258	23,8	STR	20-05-2016 20:45:00	28-07-2018 05:40:00	300
OCC-JAR-012	Jarvis	-0,368908	-160,008228	24,7	STR	11-04-2015 05:39:59	12-11-2015 22:59:59	300
OCC-JAR-013	Jarvis	-0,368944	-160,008135	14,9	STR	12-11-2015 23:03:17	20-05-2016 16:18:17	300
OCC-JAR-013	Jarvis	-0,368956	-160,008164	15,3	STR	20-05-2016 20:57:30	04-04-2017 21:17:30	300
OCC-JAR-013	Jarvis	-0,368957	-160,00814	14,9	STR	11-04-2015 02:49:59	12-11-2015 22:59:59	300
OCC-JAR-013	Jarvis	-0,369007	-160,008201	14,9	STR	05-04-2017 01:09:59	28-07-2018 18:54:59	300
OCC-JAR-013	Jarvis	-0,368995	-160,008166	14,3	STR	03-05-2012 22:55:59	10-04-2015 21:14:59	60
OCC-JAR-014	Jarvis	-0,36902	-160,008051	6,4	STR	28-03-2008 01:59:59	07-05-2008 09:59:59	1800
OCC-JAR-014	Jarvis	-0,369017	-160,008033	6,4	STR	28-03-2004 12:00:00	02-01-2006 01:00:01	1800
OCC-JAR-014	Jarvis	-0,369013	-160,008058	6,4	STR	01-04-2010 23:30:00	03-05-2012 22:00:00	1800
OCC-JAR-014	Jarvis	-0,369019	-160,008035	6,6	STR	21-03-2006 23:06:44	06-02-2007 08:06:44	1800
OCC-JAR-014	Jarvis	-0,369053	-160,008014	5,8	STR	21-05-2016 23:51:47	28-07-2018 10:26:47	300
OCC-JAR-014	Jarvis	-0,369061	-160,007994	5,8	STR	12-11-2015 23:01:50	21-05-2016 13:26:50	300
OCC-JAR-014	Jarvis	-0,369068	-160,007971	5,8	STR	11-04-2015 04:29:59	12-11-2015 22:59:59	300
OCC-JAR-014	Jarvis	-0,369038	-160,008004	5,4	STR	03-05-2012 22:36:59	10-04-2015 23:08:59	60
OCC-JAR-015	Jarvis	-0,368867	-160,008162	18,6	SBE37	05-04-2010 20:33:01	08-07-2010 10:32:02	90
OCC-JAR-016	Jarvis	-0,363274	-159,991109	9,87	STR	27-03-2008 01:00:00	04-04-2010 20:00:00	1800
OCC-JAR-016	Jarvis	-0,363233	-159,9911	9,77	STR	28-03-2004 12:00:01	20-03-2006 22:30:03	1800
OCC-JAR-016	Jarvis	-0,363246	-159,991124	9,9	STR	04-04-2010 20:30:00	04-05-2012 20:30:00	1800
OCC-JAR-016	Jarvis	-0,363246	-159,991124	9,9	STR	04-04-2010 23:49:30	05-04-2011 13:25:30	90
OCC-JAR-016	Jarvis	-0,363275	-159,99112	9,75	STR	21-03-2006 00:19:03	27-03-2008 00:19:03	1800
OCC-JAR-017	Jarvis	-0,362903	-159,9912	29,12	STR	21-03-2006 02:50:49	02-01-2008 05:50:49	1800
OCC-JAR-017	Jarvis	-0,362932	-159,991149	29,07	STR	27-03-2008 12:00:00	04-04-2010 19:30:00	1800
OCC-JAR-017	Jarvis	-0,362898	-159,99118	29,3	STR	04-04-2010 20:00:00	04-05-2012 21:30:00	1800
OCC-JAR-019	Jarvis	-0,375	-159,972283	31,13	STR	20-03-2006 23:25:36	28-03-2008 20:25:36	1800
OCC-JAR-019	Jarvis	-0,375016	-159,97228	33,21	STR	28-03-2008 21:30:00	03-04-2010 21:30:00	1800
OCC-JAR-019	Jarvis	-0,375013	-159,972268	33,2	STR	03-04-2010 22:00:00	05-05-2012 00:00:00	1800
OCC-JAR-022	Jarvis	-0,381828	-159,996632	10	STR	28-03-2004 12:00:00	21-03-2006 17:30:01	1800
OCC-JAR-022	Jarvis	-0,381844	-159,996673	10,22	STR	21-03-2006 22:43:06	12-01-2008 22:13:06	1800
OCC-JAR-022	Jarvis	-0,381844	-159,996645	10,07	STR	27-03-2008 23:00:00	03-04-2010 02:30:00	1800
OCC-JAR-022	Jarvis	-0,381847	-159,996643	10,2	STR	03-04-2010 03:00:00	03-05-2012 23:30:00	1800
OCC-JAR-022	Jarvis	-0,381847	-159,996643	10,2	STR	03-04-2010 02:58:30	16-04-2011 09:37:30	90
OCC-JAR-023	Jarvis	-0,382089	-159,99667	32,4	STR	21-03-2006 19:35:34	27-03-2008 22:05:34	1800
OCC-JAR-023	Jarvis	-0,382099	-159,996615	32,51	STR	27-03-2008 22:30:00	03-04-2010 02:00:00	1800
OCC-JAR-023	Jarvis	-0,382085	-159,996618	32,6	STR	03-04-2010 02:30:00	03-05-2012 23:30:00	1800
OCC-JAR-024	Jarvis	-0,375685	-159,974514	10,1	STR	03-04-2010 01:03:00	20-03-2011 10:51:00	90
OCC-JAR-025	Jarvis	-0,368886	-160,008083	10,1	STR	01-04-2010 23:58:30	11-04-2011 12:12:00	90
OCC-JAR-025	Jarvis	-0,369034	-160,008127	11,14	STR	01-04-2010 22:58:30	14-11-2010 00:00:00	90
OCC-JAR-026	Jarvis	-0,368938	-160,008285	32,2	STR	21-03-2006 21:57:32	28-03-2008 00:57:32	1800
OCC-JAR-026	Jarvis	-0,368928	-160,008262	32,1	STR	28-03-2008 01:00:00	01-04-2010 20:00:00	1800
OCC-JAR-026	Jarvis	-0,368905	-160,008336	31,9	STR	01-04-2010 20:30:00	03-05-2012 20:00:00	1800

Site ID	Island	Latitude (°N)	Longitude(°E)	Depth (m)	Logger type	Start	End	Sampling frequency (s)
OCC-JAR-028	Jarvis	-0,37545	-159,9745	12,2	STR	28-03-2004 12:00:00	20-03-2006 21:30:01	1800
OCC-JAR-028	Jarvis	-0,375561	-159,974305	13,1	STR	27-03-2008 21:00:00	03-04-2010 00:30:00	1800
OCC-JAR-028	Jarvis	-0,375573	-159,974321	13,4	STR	20-03-2006 21:48:08	13-07-2007 11:48:08	1800
OCC-KIN-001	Kingman	6,439351	-162,38785	25,1	STR	26-04-2015 21:34:59	07-05-2016 06:39:59	300
OCC-KIN-001	Kingman	6,439325	-162,387934	25	STR	10-05-2012 23:37:59	26-04-2015 20:22:59	60
OCC-KIN-002	Kingman	6,438725	-162,38824	13,1	STR	16-04-2010 19:40:00	27-10-2010 23:55:00	300
OCC-KIN-002	Kingman	6,438789	-162,388262	13,1	STR	20-11-2010 00:00:00	10-05-2012 20:30:00	1800
OCC-KIN-002	Kingman	6,438797	-162,388002	14,5	STR	26-04-2015 21:49:59	08-08-2018 15:04:59	300
OCC-KIN-002	Kingman	6,438817	-162,388079	14,6	STR	10-05-2012 23:36:59	26-04-2015 21:46:59	60
OCC-KIN-003	Kingman	6,437248	-162,388219	5,9	STR	27-04-2015 03:44:59	04-12-2016 16:54:59	300
OCC-KIN-003	Kingman	6,437272	-162,388245	5,8	STR	11-05-2012 00:55:59	26-04-2015 23:43:59	60
OCC-KIN-004	Kingman	6,42956	-162,382026	1,1	STR	11-05-2012 02:02:59	22-04-2015 18:35:59	60
OCC-KIN-005	Kingman	6,392413	-162,342189	7,1	STR	14-04-2010 20:00:00	12-05-2012 00:00:01	1800
OCC-KIN-005	Kingman	6,392398	-162,342184	7,5	STR	03-04-2004 00:01:01	29-03-2006 15:31:01	1800
OCC-KIN-005	Kingman	6,392402	-162,342174	7,1	STR	29-03-2006 22:42:40	05-04-2008 19:12:40	1800
OCC-KIN-005	Kingman	6,392412	-162,342173	6,81	STR	05-04-2008 21:00:00	14-04-2010 19:30:00	1800
OCC-KIN-005	Kingman	6,392517	-162,342106	7,4	STR	27-04-2015 23:14:59	08-08-2018 10:44:59	300
OCC-KIN-005	Kingman	6,392435	-162,342138	7,4	STR	12-05-2012 05:39:59	27-04-2015 18:42:59	60
OCC-KIN-007	Kingman	6,382693	-162,359274	6,7	STR	09-04-2004 06:01:00	29-03-2006 19:01:02	1800
OCC-KIN-007	Kingman	6,382683	-162,359274	6,6	STR	29-03-2006 20:01:09	04-04-2008 20:01:09	1800
OCC-KIN-007	Kingman	6,382686	-162,359286	6,5	STR	04-04-2008 21:30:00	14-04-2010 20:00:00	1800
OCC-KIN-007	Kingman	6,382683	-162,359295	6,7	STR	17-04-2010 19:00:00	11-05-2012 21:00:00	1800
OCC-KIN-007	Kingman	6,382671	-162,359312	6,9	STR	25-04-2015 08:49:59	07-08-2018 20:59:59	300
OCC-KIN-007	Kingman	6,382674	-162,359336	6,7	STR	12-05-2012 05:19:59	25-04-2015 00:18:59	60
OCC-KIN-008	Kingman	6,382138	-162,384081	23,2	STR	10-05-2012 04:02:59	24-04-2015 20:53:59	60
OCC-KIN-008	Kingman	6,382125	-162,384076	23,4	STR	24-04-2015 21:34:59	10-06-2018 00:34:59	300
OCC-KIN-009	Kingman	6,382224	-162,384065	13,4	STR	16-04-2010 12:10:00	10-05-2012 01:55:00	300
OCC-KIN-009	Kingman	6,382233	-162,383967	13,8	STR	24-04-2015 22:14:59	09-08-2018 23:14:59	300
OCC-KIN-009	Kingman	6,382256	-162,384039	14	STR	10-05-2012 04:14:59	24-04-2015 21:13:59	60
OCC-KIN-010	Kingman	6,382502	-162,384398	6,6	STR	30-03-2006 01:04:36	04-04-2008 21:34:36	1800
OCC-KIN-010	Kingman	6,382482	-162,384395	7,01	STR	05-04-2008 00:00:00	15-04-2010 20:00:00	1800
OCC-KIN-010	Kingman	6,38252	-162,384399	7,1	STR	15-04-2010 20:30:00	10-05-2012 03:00:00	1800
OCC-KIN-010	Kingman	6,382748	-162,384348	5,4	STR	24-04-2015 21:49:59	15-08-2017 20:24:59	300
OCC-KIN-010	Kingman	6,382749	-162,384364	5,2	STR	10-05-2012 06:32:59	24-04-2015 21:24:59	60
OCC-KIN-011	Kingman	6,384848	-162,377589	1,1	STR	10-05-2012 04:24:59	26-04-2015 00:49:59	60
OCC-KIN-012	Kingman	6,418761	-162,439014	24,7	STR	09-05-2012 21:26:59	25-04-2015 20:26:59	60
OCC-KIN-012	Kingman	6,418777	-162,43899	27,6	STR	26-04-2015 02:59:59	06-06-2018 23:41:06	300
OCC-KIN-013	Kingman	6,417777	-162,4382	14,6	STR	26-04-2015 05:49:59	10-08-2018 06:54:59	300
OCC-KIN-013	Kingman	6,417829	-162,438291	14,6	STR	10-05-2012 01:08:59	25-04-2015 19:53:59	60
OCC-KIN-014	Kingman	6,402154	-162,385671	14,6	STR	25-04-2015 23:59:59	07-08-2018 12:34:59	300
OCC-KIN-014	Kingman	6,402197	-162,385672	14,6	STR	10-05-2012 04:37:59	25-04-2015 22:42:59	60
OCC-KIN-015	Kingman	6,418217	-162,438716	17,69	STR	07-04-2008 21:00:00	16-04-2010 23:30:00	1800
OCC-KIN-016	Kingman	6,418873	-162,439143	33,11	STR	07-04-2008 20:30:00	16-04-2010 23:30:00	1800
OCC-KIN-016	Kingman	6,418884	-162,439155	33,3	STR	17-04-2010 00:00:00	09-05-2012 20:00:00	1800
OCC-KIN-017	Kingman	6,433221	-162,379716	8,01	STR	31-03-2006 00:56:33	06-04-2008 00:26:33	1800

Site ID	Island	Latitude (°N)	Longitude(°E)	Depth (m)	Logger type	Start	End	Sampling frequency (s)
OCC-KIN-017	Kingman	6,433207	-162,379694	8,12	STR	06-04-2008 01:00:00	16-04-2010 21:00:00	1800
OCC-KIN-017	Kingman	6,433247	-162,379715	8	STR	16-04-2010 21:30:00	10-05-2012 22:00:00	1800
OCC-KIN-018	Kingman	6,428929	-162,381776	5,39	STR	08-04-2004 06:31:00	30-03-2006 14:01:01	1800
OCC-KIN-018	Kingman	6,428882	-162,381803	5,13	STR	30-03-2006 20:31:04	07-04-2008 01:31:04	1800
OCC-KIN-018	Kingman	6,428898	-162,381794	5,19	STR	07-04-2008 02:30:00	15-04-2010 23:00:00	1800
OCC-KIN-018	Kingman	6,428923	-162,38178	5,1	STR	15-04-2010 23:30:00	11-05-2012 01:00:00	1800
OCC-KIN-019	Kingman	6,385538	-162,377408	3,38	STR	04-04-2004 00:01:01	29-03-2006 09:01:03	1800
OCC-KIN-019	Kingman	6,385517	-162,377399	3,55	STR	30-03-2006 00:20:56	04-04-2008 23:20:56	1800
OCC-KIN-019	Kingman	6,385521	-162,377399	3,87	STR	05-04-2008 01:30:00	15-04-2010 00:30:00	1800
OCC-KIN-019	Kingman	6,385537	-162,377397	3,47	STR	15-04-2010 01:00:00	09-05-2012 23:00:00	1800
OCC-KIN-020	Kingman	6,402194	-162,385259	9,85	STR	02-04-2006 19:21:34	05-04-2008 22:21:34	1800
OCC-KIN-020	Kingman	6,402185	-162,385237	10,07	STR	05-04-2008 23:00:00	14-04-2010 23:00:00	1800
OCC-KIN-020	Kingman	6,402199	-162,385229	10,1	STR	14-04-2010 23:30:00	09-05-2012 21:30:00	1800
OCC-KIN-021	Kingman	6,392409	-162,342133	0,33	SST-STR[3]	02-04-2004 23:44:51	29-03-2006 20:54:51	600
OCC-PAL-001	Palmyra	5,897525	-162,078341	29,6	STR	19-05-2012 12:00:00	18-09-2012 22:34:00	60
OCC-PAL-002	Palmyra	5,897421	-162,078342	25,6	STR	17-04-2015 07:04:59	18-05-2016 14:59:59	300
OCC-PAL-002	Palmyra	5,897442	-162,078333	25,9	STR	19-05-2016 23:59:59	05-08-2018 02:54:59	300
OCC-PAL-002	Palmyra	5,897455	-162,078339	25,5	STR	17-05-2012 20:15:59	14-06-2012 09:58:59	60
OCC-PAL-003	Palmyra	5,897302	-162,078284	14,5	STR	19-09-2012 04:45:27	16-10-2014 16:45:27	3600
OCC-PAL-003	Palmyra	5,897341	-162,078171	14,4	STR	20-05-2016 19:29:59	05-08-2018 11:04:59	300
OCC-PAL-003	Palmyra	5,897288	-162,07834	14,6	STR	17-05-2012 23:36:59	18-09-2012 20:01:59	60
OCC-PAL-003	Palmyra	5,89733	-162,078171	14,3	STR	17-04-2015 03:59:59	17-05-2016 20:44:59	300
OCC-PAL-004	Palmyra	5,89669	-162,078179	5,6	STR	19-09-2012 01:43:27	16-04-2015 20:43:27	3600
OCC-PAL-004	Palmyra	5,896948	-162,077879	6,2	STR	20-05-2016 19:49:59	25-04-2018 08:44:59	300
OCC-PAL-004	Palmyra	5,896679	-162,078181	5,5	STR	18-05-2012 01:19:59	18-09-2012 20:28:59	60
OCC-PAL-004	Palmyra	5,896953	-162,077879	5,8	STR	16-04-2015 21:34:59	19-05-2016 01:49:59	300
OCC-PAL-005	Palmyra	5,876062	-162,001955	25,7	STR	15-04-2015 22:09:59	08-06-2018 23:04:59	300
OCC-PAL-005	Palmyra	5,876094	-162,001978	26	STR	19-05-2012 23:21:59	15-04-2015 19:50:59	60
OCC-PAL-006	Palmyra	5,875603	-162,003791	15,2	STR	16-04-2015 03:14:59	23-11-2017 17:04:59	300
OCC-PAL-006	Palmyra	5,875648	-162,003912	14,8	STR	20-05-2012 02:08:59	15-04-2015 19:29:59	60
OCC-PAL-007	Palmyra	5,863563	-162,030672	24,6	STR	16-04-2015 09:34:59	30-03-2017 02:04:59	300
OCC-PAL-008	Palmyra	5,86378	-162,030634	15,6	STR	09-04-2010 00:57:30	08-08-2011 04:20:00	150
OCC-PAL-008	Palmyra	5,864228	-162,030671	10,68	STR	02-04-2008 01:30:00	09-04-2010 00:00:00	1800
OCC-PAL-008	Palmyra	5,863805	-162,030619	14	STR	16-04-2015 05:24:59	04-08-2018 03:51:26	300
OCC-PAL-009	Palmyra	5,874508	-162,040443	5,39	STR	02-04-2008 21:29:59	09-04-2010 20:30:01	1800
OCC-PAL-009	Palmyra	5,874508	-162,040414	5,8	STR	09-04-2010 21:00:00	15-05-2012 23:30:00	1800
OCC-PAL-009	Palmyra	5,874504	-162,040379	4,9	STR	15-04-2015 21:34:59	06-03-2018 18:24:59	300
OCC-PAL-009	Palmyra	5,874482	-162,040359	4,9	STR	16-05-2012 09:07:59	15-04-2015 21:14:59	60
OCC-PAL-010	Palmyra	5,870325	-162,045083	1,5	STPR	16-03-2002 19:30:00	02-06-2003 02:30:01	900
OCC-PAL-010	Palmyra	5,870297	-162,045044	1,41	STR	01-04-2004 00:01:00	14-05-2005 07:31:00	1800
OCC-PAL-010	Palmyra	5,870295	-162,045036	1,31	STR	26-03-2006 22:28:28	18-06-2007 15:58:28	1800
OCC-PAL-010	Palmyra	5,870305	-162,045067	1,51	STR	02-04-2008 02:30:00	12-04-2010 23:00:00	1800
OCC-PAL-010	Palmyra	5,870304	-162,045114	1,5	STR	12-04-2010 23:30:00	09-05-2012 02:00:00	1800
OCC-PAL-010	Palmyra	5,870307	-162,045108	1,5	STR	01-09-2017 15:27:57	04-08-2018 15:42:57	30
OCC-PAL-010	Palmyra	5,870308	-162,045094	1,6	STR	18-05-2012 07:16:59	16-04-2015 00:59:59	60

Site ID	Island	Latitude (°N)	Longitude(°E)	Depth (m)	Logger type	Start	End	Sampling frequency (s)
OCC-PAL-011	Palmyra	5,869433	-162,075215	24,53	STR	29-09-2012 00:36:51	17-04-2015 19:36:53	3600
OCC-PAL-011	Palmyra	5,869458	-162,075245	24,4	STR	17-04-2015 23:39:59	07-07-2018 20:44:59	300
OCC-PAL-011	Palmyra	5,869458	-162,075245	24,4	STR	19-05-2016 12:04:59	06-08-2018 12:09:59	300
OCC-PAL-011	Palmyra	5,869418	-162,07522	25	STR	15-05-2012 22:15:59	28-09-2012 22:36:59	60
OCC-PAL-012	Palmyra	5,869598	-162,075129	14,7	STR	28-09-2012 23:50:31	23-02-2015 08:50:31	3600
OCC-PAL-012	Palmyra	5,869606	-162,075107	14,2	STR	18-04-2015 02:24:59	18-05-2016 09:49:59	300
OCC-PAL-012	Palmyra	5,869736	-162,075496	14,2	STR	19-05-2016 15:59:59	06-08-2018 06:54:59	300
OCC-PAL-012	Palmyra	5,869594	-162,07514	14,6	STR	15-05-2012 21:41:59	28-09-2012 23:37:59	60
OCC-PAL-013	Palmyra	5,870118	-162,075097	5,5	STR	02-10-2012 20:47:21	20-08-2014 09:47:21	3600
OCC-PAL-013	Palmyra	5,870139	-162,075118	4,9	STR	18-04-2015 03:14:59	17-05-2016 11:39:59	300
OCC-PAL-013	Palmyra	5,870108	-162,075086	5	STR	15-05-2012 21:08:59	28-09-2012 23:37:59	60
OCC-PAL-015	Palmyra	5,863967	-162,126958	15,2	STR	02-04-2004 00:01:02	28-03-2006 00:31:02	1800
OCC-PAL-015	Palmyra	5,864062	-162,126973	15,33	STR	06-10-2009 00:00:00	07-04-2010 19:00:00	1800
OCC-PAL-015	Palmyra	5,86415	-162,126986	15,5	STR	07-04-2010 19:00:00	14-05-2012 21:00:00	1800
OCC-PAL-015	Palmyra	5,864103	-162,126939	15,2	STR	18-04-2015 03:14:59	03-08-2018 05:29:59	300
OCC-PAL-015	Palmyra	5,864145	-162,126988	15,4	STR	15-05-2012 00:01:59	18-04-2015 01:06:59	60
OCC-PAL-016	Palmyra	5,88398	-162,168891	24,7	STR	20-04-2015 18:34:59	01-08-2018 23:54:59	300
OCC-PAL-016	Palmyra	5,883987	-162,16889	24,9	STR	19-05-2012 03:26:59	19-04-2015 20:13:59	60
OCC-PAL-017	Palmyra	5,883225	-162,13321	14,5	STR	19-04-2015 00:44:59	28-10-2017 06:54:59	300
OCC-PAL-018	Palmyra	5,882432	-162,121279	3,87	STR	03-04-2008 01:30:00	11-04-2010 01:00:00	1800
OCC-PAL-018	Palmyra	5,88247	-162,121345	4,6	STR	21-05-2016 03:09:59	02-08-2018 07:04:59	300
OCC-PAL-018	Palmyra	5,882459	-162,121347	4,6	STR	17-05-2012 06:05:59	18-04-2015 14:42:59	60
OCC-PAL-018	Palmyra	5,882479	-162,121339	4,6	STR	19-04-2015 06:04:59	20-05-2016 10:39:59	300
OCC-PAL-021	Palmyra	5,891878	-162,12242	0,9	STR	19-05-2012 20:00:00	08-09-2014 15:00:00	3600
OCC-PAL-021	Palmyra	5,891894	-162,122452	0,8	STR	20-04-2015 04:34:59	02-12-2016 17:24:59	300
OCC-PAL-022	Palmyra	5,886245	-162,085904	3,58	STR	02-04-2004 03:01:01	25-03-2006 01:01:03	1800
OCC-PAL-022	Palmyra	5,88624	-162,085886	3,32	STR	25-03-2006 01:46:09	15-11-2007 18:16:09	1800
OCC-PAL-022	Palmyra	5,886221	-162,085897	3,37	STR	03-04-2008 00:30:00	08-04-2010 21:30:00	1800
OCC-PAL-022	Palmyra	5,886195	-162,085932	3,4	STR	17-05-2012 02:00:00	22-04-2015 07:00:00	3600
OCC-PAL-022	Palmyra	5,886047	-162,086089	3,4	STR	23-04-2015 01:09:59	06-08-2018 03:24:59	300
OCC-PAL-027	Palmyra	5,869354	-162,075254	30,2	STR	19-05-2012 12:00:00	28-09-2012 23:38:00	60
OCC-PAL-028	Palmyra	5,89713	-162,078286	10,1	STR	17-05-2012 23:06:59	18-09-2012 00:33:59	60
OCC-PAL-029	Palmyra	5,897374	-162,078338	19,1	STR	17-05-2012 22:50:59	18-09-2012 11:23:59	60
OCC-PAL-030	Palmyra	5,882758	-162,06182	4,38	STR	01-04-2008 02:00:00	01-12-2009 03:15:06	1800
OCC-PAL-030	Palmyra	5,882774	-162,061827	4,26	STR	24-03-2006 21:46:05	30-03-2008 12:16:05	1800
OCC-PAL-030	Palmyra	5,882752	-162,061842	4,5	STR	11-04-2010 00:00:00	16-05-2012 23:00:00	1800
OCC-PAL-031	Palmyra	5,869727	-162,075153	10,7	STR	15-05-2012 21:30:59	28-09-2012 23:37:59	60
OCC-PAL-032	Palmyra	5,869528	-162,075166	19,5	STR	15-05-2012 21:43:59	28-09-2012 22:51:59	60
OCC-PAL-033	Palmyra	5,874508	-162,040443	0,19	SST-STR	02-04-2008 21:30:00	24-11-2009 02:30:00	1800
OCC-PAL-034	Palmyra	5,87611	-162,00237	20,6	SBE37	14-04-2010 14:40:01	16-05-2011 23:45:02	150
OCC-PAL-034	Palmyra	5,87611	-162,00237	21,1	STR	13-04-2010 23:00:00	15-05-2012 00:30:00	1800
OCC-PAL-034	Palmyra	5,876111	-162,002369	18,89	STR	02-04-2008 22:30:00	13-04-2010 22:30:00	1800
OCC-PAL-035	Palmyra	5,87637	-162,00206	32,5	STR	12-04-2010 21:30:00	27-03-2012 21:30:00	1800
OCC-PAL-035	Palmyra	5,876367	-162,002059	32,61	STR	02-04-2008 22:00:00	12-04-2010 21:00:00	1800
OCC-PAL-036	Palmyra	5,88383	-162,168568	19,2	SBE37	16-04-2010 04:37:31	16-05-2011 23:45:03	150

Site ID	Island	Latitude (°N)	Longitude(°E)	Depth (m)	Logger type	Start	End	Sampling frequency (s)
OCC-PAL-036	Palmyra	5,883783	-162,168585	19,41	STR	31-03-2008 22:30:00	11-04-2010 22:00:00	1800
OCC-PAL-036	Palmyra	5,88383	-162,168568	19,2	STR	11-04-2010 22:30:00	18-05-2012 20:30:00	1800
OCC-PAL-037	Palmyra	5,884125	-162,169101	32,91	STR	31-03-2008 22:00:00	11-04-2010 21:00:00	1800
OCC-PAL-037	Palmyra	5,884095	-162,169059	32,8	STR	11-04-2010 21:30:00	18-05-2012 20:00:00	1800
OCC-PAL-038	Palmyra	5,882062	-162,062363	25,19	STR	24-03-2006 23:14:59	27-02-2008 15:14:59	1800
OCC-PAL-038	Palmyra	5,882037	-162,062354	25,19	STR	01-04-2008 02:00:00	10-04-2010 23:00:00	1800
OCC-PAL-038	Palmyra	5,882084	-162,062356	25,6	STR	10-04-2010 23:30:00	09-01-2014 13:30:00	1800
OCC-PAL-041	Palmyra	5,882429	-162,033001	10,4	STR	09-04-2010 19:30:00	16-08-2011 06:32:30	150
OCC-PAL-042	Palmyra	5,882775	-162,032983	14,6	STR	10-04-2010 12:00:00	14-09-2011 11:17:30	150
OCC-PAL-043	Palmyra	5,882934	-162,032928	19,6	SBE37	16-04-2010 04:37:30	16-05-2011 23:45:04	150
OCC-PAL-044	Palmyra	5,864452	-162,031769	10,1	STR	09-04-2010 08:10:00	01-11-2011 10:07:30	150
OCC-PAL-045	Palmyra	5,864227	-162,030652	9,75	STR	27-03-2006 23:20:05	02-03-2008 22:50:05	1800
OCC-PAL-045	Palmyra	5,864258	-162,030704	10,1	STR	09-04-2010 00:17:30	22-09-2011 03:37:30	150
OCC-PAL-045	Palmyra	5,864258	-162,030704	10,1	STR	09-04-2010 00:30:00	15-05-2012 02:30:00	1800
OCC-PAL-046	Palmyra	5,863655	-162,030592	18,9	SBE37	16-04-2010 04:37:31	16-05-2011 23:45:02	150
OCC-PAL-047	Palmyra	5,866383	-162,113638	19,3	STR	18-09-2009 22:39:00	08-04-2010 20:27:00	90
OCC-PAL-047	Palmyra	5,866403	-162,113658	19,6	STR	08-04-2010 20:30:00	15-05-2012 00:00:00	1800
OCC-PAL-048	Palmyra	5,866544	-162,112766	12,2	STR	08-04-2010 20:00:00	15-05-2012 00:00:00	1800
OCC-PAL-048	Palmyra	5,866562	-162,112751	12,19	STR	18-09-2009 22:48:00	08-04-2010 19:33:00	90
OCC-PAL-049	Palmyra	5,866482	-162,113624	14,67	STR	08-04-2010 02:20:00	25-10-2010 23:57:30	150
OCC-PAL-049	Palmyra	5,866467	-162,113515	13,61	STR	18-09-2009 22:33:00	08-04-2010 02:19:30	90
OCC-PAL-050	Palmyra	5,896388	-162,128132	11,3	STR	08-04-2010 00:37:30	23-08-2011 10:02:30	150
OCC-PAL-050	Palmyra	5,896363	-162,128171	11,08	STR	16-09-2009 21:19:30	08-04-2010 00:31:30	90
OCC-PAL-051	Palmyra	5,896426	-162,127251	10,7	STR	08-04-2010 00:10:00	24-07-2010 11:55:00	150
OCC-PAL-051	Palmyra	5,896454	-162,127226	10,17	STR	16-09-2009 21:15:00	08-04-2010 00:09:00	90
OCC-PAL-053	Palmyra	5,897099	-162,12831	21,2	SBE37	14-04-2010 14:40:01	16-05-2011 23:47:31	150
OCC-PAL-053	Palmyra	5,897103	-162,128218	20,61	STR	16-09-2009 21:24:00	07-04-2010 23:22:30	90
OCC-PAL-055	Palmyra	5,866668	-162,126519	10,3	STR	07-04-2010 21:22:30	03-05-2011 02:55:00	150
OCC-PAL-056	Palmyra	5,86089	-162,126709	20,4	SBE37	14-04-2010 14:40:01	16-05-2011 23:45:03	150
OCC-PAL-057	Palmyra	5,884613	-162,102852	9,13	STR	01-04-2008 22:59:59	10-04-2010 20:30:01	1800
OCC-PAL-057	Palmyra	5,884665	-162,102831	9,11	STR	25-03-2006 23:42:55	01-04-2008 21:12:55	1800
OCC-PAL-058	Palmyra	5,884665	-162,102831	1	SBE37	26-03-2006 12:59:53	01-04-2008 20:59:54	1800
OCC-PAL-058	Palmyra	5,884683	-162,102833	0,67	SBE37	15-03-2002 04:29:28	23-10-2002 23:59:28	900
OCC-PAL-058	Palmyra	5,884613	-162,102852	1	SBE37	01-04-2008 23:00:01	10-04-2010 19:00:02	1800
OCC-PAL-058	Palmyra	5,884674	-162,102813	1	SBE37	30-03-2004 22:30:00	25-03-2006 20:30:01	1800
OCC-PAL-058	Palmyra	5,884613	-162,102852	1	STR	01-04-2008 23:00:00	15-05-2009 22:00:00	1800
OCC-PAL-058	Palmyra	5,884665	-162,102831	0,97	STR	26-03-2006 00:00:22	17-10-2007 12:30:23	1799
OCC-PAL-058	Palmyra	5,884674	-162,102813	1	STR	30-03-2004 23:01:03	25-03-2006 18:01:03	3600
OCC-PAL-059	Palmyra	5,88235	-162,062168	15,84	STR	24-03-2006 22:55:05	08-01-2008 02:26:31	1800
OCC-PAL-060	Palmyra	5,882783	-162,061833	0,19	SST-STR	24-03-2006 21:30:00	14-05-2007 21:00:00	1800